Preprint Title	Surface functionalized drug loaded spinel ferrite MFe$_2$O$_4$ (M = Fe, Co, Ni, Zn) nanoparticles, their biocompatibility and cytotoxicity *in vitro*: A comparison
Authors	Sadaf Mushtaq, Khuram Shahzad, Tariq Saeed, Anwar Ul-Hamid, Bilal H. Abbasi, Nafees Ahmad, Waqas Khalid, Muhammad Atif, Zulqurnain Ali and Rashda Abbasi
Publication Date	10 Aug. 2021
Article Type	Full Research Paper
ORCID® iDs	Sadaf Mushtaq - https://orcid.org/0000-0002-9990-2164; Anwar Ul-Hamid - https://orcid.org/0000-0002-0259-301X; Bilal H. Abbasi - https://orcid.org/0000-0002-6529-2134; Zulqurnain Ali - https://orcid.org/0000-0001-5912-5957; Rashda Abbasi - https://orcid.org/0000-0002-0268-0359

Surface functionalized drug loaded spinel ferrite MFe₂O₄ (M = Fe, Co, Ni, Zn) nanoparticles, their biocompatibility and cytotoxicity *in vitro*: A comparison

Sadaf Mushtaq[1,2], Khuram Shahzad[3], Tariq Saeed[1], Anwar Ul-Hamid[4], Bilal Haider Abbasi[2], Nafees Ahmad[1], Waqas Khalid[3], Muhammad Atif[3], Zulqurnain Ali[3], Rashda Abbasi[1*]

[1]Institute of Biomedical and Genetic Engineering, G-9/1, Islamabad, Pakistan

[2]Department of Biotechnology, Quaid-i-Azam University, Islamabad, Pakistan

[3]Department of Physics, Functional Materials Lab, Air University, Sector E-9, Islamabad, Pakistan

[4]Core Research Facilities, King Fahd University of Petroleum & Minerals, Dhahran 31261, Saudi Arabia

[*]Corresponding author:

Rashda Abbasi

Functional Genomics, Institute of Biomedical and Genetic Engineering (IBGE)

Islamabad, Pakistan.

Tel.: +92 51 9106281; fax: +92 51 9106283

Email: r.abbasi@daad-alumni.de

Abstract

In this study, polymer coated biocompatible MFe_2O_4 (M=Fe, Co, Ni, Zn) NPs were developed as carriers of anticancer drugs. Synthesized NPs were characterized via XRD, TEM, EDS and PPMS which confirmed formation of pure cubic structures (14 - 22 nm) with magnetic properties. The anticancer drugs: doxorubicin (DOX) and methotrexate (MTX) loaded NPs exhibited tumor specificity with significantly higher ($p<0.005$) drug release in acidic pH 5.5. NPs were highly colloidal in deionized water, PBS and SBB (-35 to -26 mV). They showed elevated and dose dependent cytotoxicity *in vitro* compared to free drug controls. IC_{50} values ranged from 0.81 - 3.97 μg/ml against HepG2 and HT144 cells. On the contrary, IC_{50} values for normal lymphocytes were 10 to 35 times higher (18.35 - 43.04 μg/ml). CFO and ZFO nanocarriers were highly genotoxic ($p<0.05$) against both cancer cell lines. NPs caused cytotoxicity via oxidative stress, causing DNA damage and activation of p53 (significantly elevated expression, $p<0.005$) mediated cell cycle arrest (majorly G1 and G2/M arrest) and apoptosis. When tested for cytotoxicity in 3D spheroids, they showed significant ($p<0.05$) reduction in spheroid diameter and upto $74 \pm 8.9\%$ cell death after 2 weeks. In addition, they also inhibited MDR pump activity in both cell lines suggesting their potential to combat multidrug resistance in cancers. Among tested MFe_2O_4 NPs, CFO nanocarriers were most favorable for targeted cancer therapy due to excellent magnetic, colloidal, cytotoxic, and biocompatible aspects. However, detailed investigations of molecular pathways involved, *in vivo* cytotoxicity and magnetic field assisted experiments are needed to fully exploit them in therapeutic domains.

Keywords: Magnetic spinel ferrite nanoparticles, polyisobutylene-alt-maleic anhydride, drug carriers, doxorubicin, methotrexate, *in vitro*

Introduction

Cancer being the second leading cause of death, is a global health concern [1, 2]. It is caused by uncontrolled cell proliferation or reduced rate of cell death or both [3]. Conventional treatment strategies for cancer including surgery, radiotherapy and chemotherapy lack the ability to selectively target neoplastic tissue resulting in systemic toxicity [4]. Due to which, focus is now transferred towards nanomedicine which enables targeted therapy and reduces side effects of conventional therapeutic agents [5]. Functionalized nanoparticles have the potential to improve therapeutic performance of drugs by regulation of pharmacokinetics and pharmacodynamics [6, 7]. Moreover, water compatibility of nanocarriers provides better chemical stability and bioavailability of the drug which allows controlled release. Additionally, attached drug is protected from degradation allowing increased circulation time [8]. Targeting of specific tumor tissue is therefore achieved by increased biodistribution process known as Enhanced Permeability and Retention (EPR) effect [9].

 Magnetic nanoparticles (MNPs) have gained prodigious attention as effective drug delivery systems due to their distinct physiochemical attributes, high surface to volume ratio, and possibility of surface functionalization [10]. Furthermore, feasibility of magnetic field assisted control of MNPs behavior has proven them suitable candidates for targeted drug delivery [11], hyperthermia [12], biosensors [13], magnetic resonance imaging (MRI) [14] and magnetic separation [15]. Magnetite (Fe_3O_4) nanoparticles (NPs) belonging to spinel ferrite class, are the most extensively studied MNPs for clinical applications and many of them have been approved by Food and Drug Administration (FDA). Their intended applications include hyperthermia, disease diagnosis, MRI contrasting agents and tackling iron deficiencies [16, 17]. Aside from

their useful applications, magnetite NPs have some serious shortcomings such as chemical reactivity, rapid oxidation, particle agglomeration and high surface energy which may affect their biocompatibility and performance [16, 18]. Moreover, they have poor magnetization at smaller size and presence of iron has been associated with adverse interaction with hemoglobin [18, 19].

Magnetic spinel ferrites nanoparticles (MSFNPs) with general formula MFe_2O_4 (where M = divalent cation of Co, Ni, Zn, Mn or Mg) are soft magnetic materials having a face-centered cubic structure [20]. Cobalt ferrite NPs among them, have large magneto crystalline anisotropy, high saturation magnetization and coercivity even at room temperature as compared to others [21]. Substitution of metal cations M^+ such as cobalt, nickel, and zinc (Co, Ni, Zn) will contribute towards diverse magnetic properties, morphology and size of iron oxide NPs [18, 22, 23] along with varied tissue penetration and hemocompatibility which can be useful for biomedical applications [17, 24, 25].

Furthermore, in order to be exploited in biomedical domain, NPs need to fulfill certain criteria which includes water-solubility, excellent colloidal stability, biocompatibility, and high saturation magnetization which enables controlled and non-toxic biological interactions [26]. Hydrophilicity of nanocarriers is important, as native hydrophobic surface of NPs are rapidly opsonized by hydrophobic serum proteins [27]. For this, surface functionalization has a major role [28, 29]. It alters surface chemistry of NPs, thereby affecting their physiochemical and biological properties [16, 17, 30, 31].

In the present work, we have synthesized a variety of MFe_2O_4 (M = Co, Ni and Zn,) NPs using sono-chemical technique. Particle agglomeration was prevented by using oleic acid as surfactant [32]. Phase change of hydrophobic NPs was achieved by functionalization with amphiphilic brush copolymer, poly (isobutylene-alt-maleic anhydride) implanted with

4

dodecylamine (PMA), providing biocompatibility, colloidal stability and hydrophilicity [33, 34]. It is composed of hydrophobic side chains and the backbone of hydrophilic groups. The hydrophobic side chains interact with hydrophobic surfactant (oleic acid) present on NPs surface thereby, exposing hydrophilic end to interact with the aqueous environment and contributing towards colloidal nano-suspension [26, 28, 35]. NPs surface was further functionalized with anticancer drugs; doxorubicin (DOX) and methotrexate (MTX) via 1-Ethyl-3-(3-dimethylaminopropyl) carbodiimide (EDC) chemistry. Our aim was to compare biocompatibility, colloidal stability, and *in vitro* cytotoxicity of these nanocarriers for potential anticancer drug delivery.

2. Results and Discussion

2.1 Physical characterizations

The XRD data of all samples was analyzed using Rietveld refinement techniques by Fullprof Suit program. The data was refined according to their space groups. The rietveld refined XRD pattern of MFe_2O_4 nanoparticles (Fig. 1a) are marked as triangle indicating experimental data with red solid line marked calculated intensities. The difference between two intensities were marked with blue line at bottom of graph and Bragg's peak positions are marked vertical lines according to their space groups. All the observed peaks are allowed the Bragg's 2θ positions. The background was refined using pseudo voigt function by taking atomic fractional positions as fixed parameters during refinement, however some factors such as lattice constant, isothermal parameters, scale, and shape factors are considered as free parameters. All the samples show low value of goodness of fit (χ^2). Several physical parameters (lattice constant, average crystalline size, density) were calculated as given in Table 1. The prominent peaks originating from different planes (111, 220, 311, 222, 400, 422, 440, 533, 620), were found in good agreement with standard JCPDS cards (019-0629, 22-1086, 10-0325, and 82-1049 for M

= Fe, Co, Ni, Zn respectively). Slight peak shift at (311) plane was observed for CFO, NFO and ZFO as compared to FeO due to the ionic radii difference of divalent cations M^{+2}. Peak shift also indicates the incorporation of M^{+2} cations into the lattice. Further confirmation of crystalline nature of composites was obtained by selected area electron diffraction (SAED) patterns. The SAED images explain the position of crystalline system upon diffraction. The results further provide the concentric rings that explains the different hkl planes as explained in Fig. 1b. Furthermore, the formation of cubic phase of samples is consistent with XRD results.

Table 1: Different physical parameters calculated form XRD analysis.

Nanostructures	Crystallite size (nm)	Lattice constant (A°)	Goodness of fit (χ^2)
FeO	27	8.43	2.03
CFO	23	8.39	2.11
NFO	33	8.35	2.53
ZFO	24	8.46	2.37

Formation of spherical NPs was confirmed by TEM results (Fig. 1c). The nanospheres are uniformally distributed throughout the surface of samples. High resolution TEM images show the crystalline structure with edges of single grain of nanoparticles. The inter planner distance was meaured for each sample with marked lattice fringes with respective planes. Average particle size was found to be 16 - 21 nm for FeO, 14 - 18 nm for CFO, and 12 - 16 nm for NFO with d spacing value (0.47 nm, 0.25 nm, 0.24 nm, 0.20 nm) for FeO, CFO, NFO and ZFO respectively, crossponding to (111), (311), (311), and (400) respectively. These planes are well

matched with the inter planner distance of diffraction pattern standards obtained from their standard JCPDS database.

Weight and atomic % of M:Fe ions in all samples as studied by energy dispersive spectroscopy (EDS) is given in Table 2. No extra impurity peaks were present in the spectrum (Fig. 1d) due to use of coprecipitation synthesis method in which samples were washed several times to remove any impurity.

Table 2: EDS analysis showing elemental composition for MFe_2O_4 (M = Fe, Co, Ni, Zn) NPs

	FeO		CFO			NFO			ZFO		
	O	Fe	O	Fe	Co	O	Fe	Ni	O K	Fe	Zn
Atomic %	63.66	36.34	63.30	24.28	12.43	63.26	24.20	12.55	69.38	20.41	10.21
Weight %	33.42	66.58	36.76	46.29	16.96	37.50	48.33	14.17	40.22	42.86	16.91
Total	**100**		**100**			**100**			**100**		

The physical property measurement system (PPMS) was used for evaluating magnetic properties of MFe_2O_4 NPs. Hysteresis loops were measured at room temperature on 2 T applied field. The samples have clearly shown ferromagnetic behavior with different saturation magnetizations Ms (emu/g) and coercivity Hc (Oe) as shown in Table 3 [36]. From Fig. 1e, all samples have gone through saturation at 2 T applied field except nickel ferrite, this may be due to the presence of strong magnetic anisotropy that required higher applied field to saturate [37]. Cobalt ferrite has maximum coercivity (883 Oe) and saturation magnetization values (56

emu/g) than other ferrites due to high anisotropy. Also, during cationic distribution, Co^{+2} cations incorporate in the Fe-O whereas, cationic distribution for other divalent metals Ni^{+2} or Zn^{+2} decreases the magnetic anisotropy [24, 38]. Moreover zinc ferrite has slightly increased coercivity than nickel ferrite and iron oxide due to the formation of noncollinear ferrimagnetic structure [39]. From Table 3, cobalt ferrite has the best magnetic properties in terms of saturation magnetization and coercivity followed by iron, nickel and zinc ferrite. Furthermore, polymer coated nanoparticles exhibit a small change in saturation magnetization, which is still enough to manipulate NPs using external magnetic field [40].

Table 3: Magnetic parameters analysis for MFe_2O_4 (M = Fe, Co, Ni, Zn) nanoparticles.

|	Saturation Magnetization M_S (emu/g)	Remanence Value M_R (emu/g)	Coercivity Hc (Oe)
FeO	34	6.2	35
CFO	56	22	883
NFO	39	0.32	10
ZFO	25	9.21	179

The uniform size distribution of the MFe_2O_4 (M = Fe, Co, Zn, Ni) NPs was confirmed by agarose gel electrophoresis. All samples moved towards positive potential due to negatively charged PMA coating (Fig. 1f).

The colloidal stability (hydrodynamic size, surface charge, and polydispersity index PDI) of NPs was assessed using DLS. All NPs (polymer coated, and drug attached) dispersed in

deionized water, SBB pH 9.0, PBS pH 7.4 and DMEM were used for zeta potential measurements. The purpose of using buffers (SBB, PBS) was to get indirect surface charge information, deionized water to check the influence of electrolytes on NPs stability [41], and DMEM as representative of biological assays. All NPs (MFe_2O_4-PMA and MFe_2O_4 +DOX and +MTX) indicated the higher values for zeta potential (-35 to -26 mV) in all dispersion media except DMEM (-17 to -10 mV) as shown in Table 4. The reason behind lower values of zeta potential is interaction of NPs with serum proteins present in DMEM [42, 43]. In cell culture medium, NPs agglomerate with serum proteins and are therefore recruited in cell via protein corona effect which increases the bioavailability of NPs by many folds [44, 45]. Polymer coated samples have less hydrodynamic size (60 - 93 nm) as compared to drug loaded samples (74 - 110 nm), which was further increased (132 - 210 nm) in DMEM due to interaction of proteins with samples. NFO among them, has largest hydrodynamic size (> 200 nm) in DMEM, which is not considered suitable for biological applications [43, 46]. All samples have lower values (0.13 - 0.33) of polydispersity index (PDI) which indicates uniform distribution of NPs in different dispersion media.

Table 4: Zeta potential, z-average hydrodynamic diameter (D_z), and PDI values of MFe_2O_4 (M = Fe, Co, Zn, Ni) NPs by DLS.

Sample	Zeta Potential (mV) ± SD				Hydrodynamic size (nm) ± SD				PDI			
	Water	SB	PBS	DMEM	Water	SB	PBS	DMEM	Water	SB	PBS	DMEM
FeO-PMA	-33±1.1	-31±1.3	-26±1.9	-17±2.1	46±3	66±4	64±4	132±5	0.21	0.29	0.20	0.37
FeO+DOX	-29±1.7	-25±1.4	-25±1.1	-15±1.8	85±3	84±5	110±2	152±8	0.27	0.25	0.21	0.45
FeO+MTX	-33±1.6	-31±1.9	-27±1.9	-16±1.9	91±3	89±5	116±3	157±6	0.24	0.27	0.29	0.46
CFO-PMA	-35±1.8	-27±1.5	-31±1.6	-17±1.3	46±3	62±2	70±5	86±3	0.13	0.17	0.27	0.37
CFO+DOX	-32±1.1	-29±1.6	-27±0.9	-15±1.7	74±6	83±5	92±4	117±7	0.19	0.21	0.29	0.49
CFO+MTX	-31±1.3	-26±1.2	-26±1.6	-14±1.6	64±2	89±7	99±3	145±5	0.18	0.20	0.31	0.46
NFO-PMA	-25±1.1	-23±1.0	-27±0.7	-13±1.2	84±6	92±3	160±4	151±8	0.26	0.35	0.33	0.41
NFO+DOX	-24±1.2	-21±2.1	-23±2.6	-10±1.3	104±6	108±3	163±7	203±5	0.33	0.41	0.41	0.51
NFO+MTX	-21±1.1	-20±2.3	-24±1.9	-11±1.5	110±6	129±5	157±6	210±3	0.31	0.39	0.42	0.67
ZFO-PMA	-34±1.6	-29±1.9	-29±1.3	-17±2.3	54±5	65±4	93±1	135±6	0.18	0.15	0.20	0.39
ZFO+DOX	-30±1.3	-29±2.2	-28±1.9	-16±1.9	74±3	86±5	121±4	153±6	0.19	0.17	0.27	0.41
ZFO+MTX	-31±1.7	-27±1.5	-27±1.5	-13±1.8	79±4	93±4	110±3	157±8	0.19	0.21	0.29	0.46
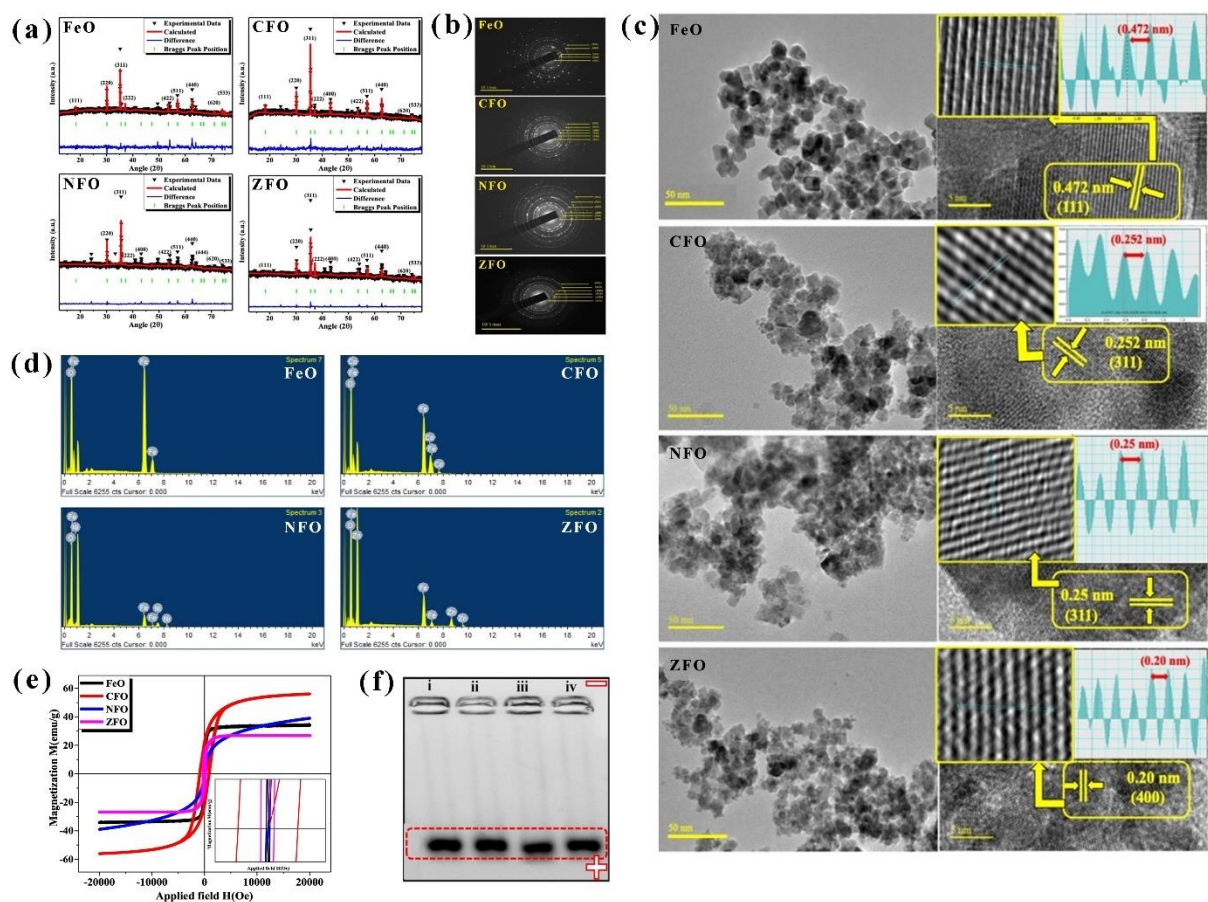
Figure 1: Physical characterizations of MFe$_2$O$_4$ (M=Fe, Co, Ni, Zn) NPs. **(a)** Rietveld-refined XRD pattern with SAED images explaining different hkl planes. The triangles represent experimental points, and the solid line represents Rietveld-refined data. The bottom line shows the difference between the experimental and refined data. **(b)** The marked 2θ positions are the allowed Bragg peaks. **(c)** TEM micrographs with HR-TEM showing respective planes **(d)** EDS analysis showing major elemental composition in synthesized NPs. **(e)** Magnetization vs. applied field on MFe$_2$O$_4$ (M = Fe, Co, Zn, Ni) NPs at room temperature on 2 T applied field. **(f)** Agarose gel electrophoresis image of **(i)** FeO-PMA **(ii)** NFO-PMA **(iii)** CFO-PMA **(iv)** ZFO-PMA NPs. Black bands on gel indicate uniform size distribution and negative surface charge on colloidal NPs.

2.2 Drug loading and drug release kinetics (pH dependent)

The UV-Vis based confirmation of drug (DOX and MTX) attachment with PMA coated MFe_2O_4 (M = Fe, Co, Zn, Ni) NPs is shown in Fig. 2a. Samples were washed and concentrated with centrifugal filters many times to remove unattached drug. Attached DOX and MTX were indicated at 480 and 372 nm respectively. NPs-PMA, drug only and centrifugal filter wastes were also included for comparison. We used 0.5 mM drugs for loading on NPs. The encapsulated and loaded drug % for DOX and MTX are given in Table 5.

Table 5: Drug (encapsulation efficiency EE and loading capacity LC) % of MFe_2O_4 (M = Fe, Co, Ni, Zn) nanoparticles.

Nanoparticles	EE % DOX	EE (uM) at 5 ug/mL	EE % MTX	EE (uM) at 5 ug/mL	LC % DOX	LC % MTX
FeO	79	0.08	83	0.08	39	41
CFO	84	0.21	82	0.21	42	46
NFO	78	0.09	80	0.10	37	40
ZFO	79	0.09	82	0.10	43	45

For pH dependent drug release kinetics, drug loaded NPs were dispersed in different pH solutions (1X PBS; pH 5.5, 6.5 and 7.4) at room temperature and release % was investigated over a time interval (0 - 120 minutes). A strong pH dependent drug release was observed at lower pH of 5.5 ($p < 0.005$) in all samples. For the drug loaded NPs, burst release of drug was observed within initial 5 - 10 minutes (Fig. 2 (b - c)) which indicates that the amide bonds between the drug molecules and NPs were acid labile in nature resulting in detachment of drug

from NPs under acidic conditions (pH. 5.5) [47]. The drug release became slower and sustained after that. The lower pH or acidic conditions change the surface charge density that causes deionization of amide bond, resulting in drug release [48, 49]. From MFe_2O_4 (M = Fe, Co, Zn, Ni) NPs, CFO had highest total drug release for DOX and MTX (percent release = 62 ± 0.99 & 59 ± 1.19, respectively) at lower pH (5.5), followed by ZFO, FeO and NFO as shown in Table 6. The drug release behavior at pH (7.4, 6.5, and 5.5) for DOX and MTX shows increasing curve from higher pH (7.4) to lower pH (5.5). Small amount of release (20 - 30%) for DOX and MTX was observed at pH (7.4), which indicates that the pH-dependent release behavior may contribute towards efficient drug delivery at tumor sites where acidic microenvironment is prevalent [50] with lesser pre-mature drug release in circulation and normal cells where pH is maintained at 7.4. Furthermore, once NPs are internalized by tumor cells, the acidic environment in the endosome may also trigger hydrolysis of amide bond present between drug and polymer, thereby rapidly releasing drug from NPs in cytosol [51].

Table 6: Total drug (DOX/MTX) release from MFe_2O_4 (M = Fe, Co, Zn, Ni) nanoparticles, at pH 5.5, 6.5, and 7.4 after 120 minutes.

Nanoparticles	DOX			MTX		
	pH 5.5	**pH 6.5**	**pH 7.4**	**pH 5.5**	**pH 6.5**	**pH 7.4**
FeO	54 ± 1.05	45 ± 1.23	30 ± 0.89	52 ± 1.15	46 ± 1.11	23 ± 0.87
CFO	62 ± 0.99	49 ± 1.11	29 ± 1.09	59 ± 1.19	49 ± 0.91	26 ± 1.12
NFO	51 ± 1.02	40 ± 0.90	25 ± 0.92	52 ± 1.08	43 ± 1.07	19 ± 0.91
ZFO	57 ± 1.30	46 ± 1.22	25 ± 1.23	54 ± 1.16	45 ± 0.99	25 ± 0.92

(a)

(b)

(c)
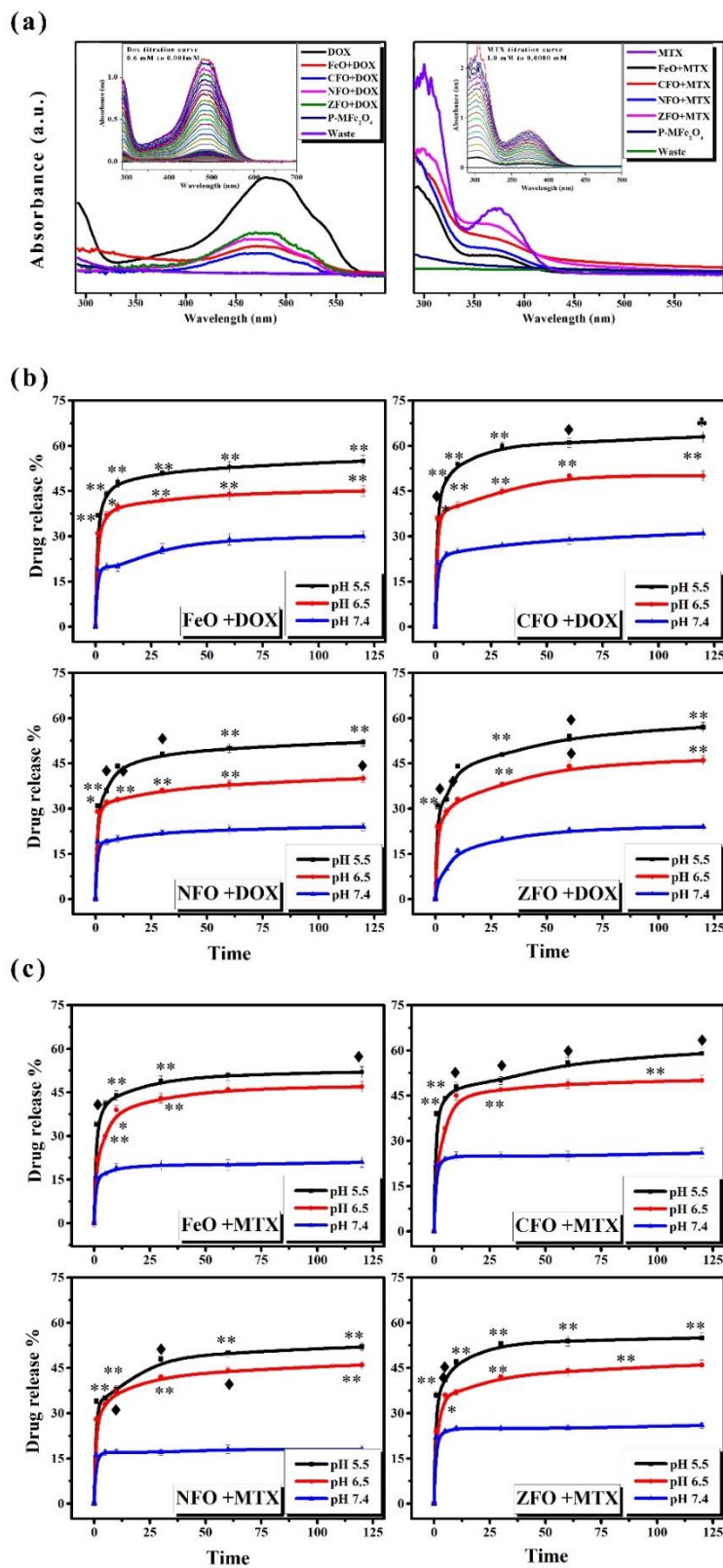
Figure 2: (a) UV-Vis absorbance plot of DOX and MTX loaded MFe_2O_4 (M = Fe, Co, Zn, Ni) NPs **(b)** Drug release kinetics of DOX and **(c)** MTX loaded MFe_2O_4 NPs at pH 5.5, 6.5, and 7.4 and different time intervals (0, 1, 5, 10, 20, 40, 60 and 120 minutes). Results indicate mean $\pm$ SD of three independent experiments. $^*p<0.05$, $^{**}p<0.005$, $^♣p<0.01$ and $^♦p<0.001$ (paired two tailed t-test when compared to pH 7.4).

2.3 Functionalized MFe_2O_4 NPs cause cytotoxicity *in vitro*

SRB assay was performed using HepG2 and HT144 cells *in vitro* to screen cytotoxic potential of functionalized MFe_2O_4 NPs where M = Fe, Co, Ni, Zn. Cells were exposed to 5 µg/ml of NPs for 24 hours. For better comparison, free drug (DOX and MTX) controls were included, which were equivalent to total drug attached with said dose of NPs as mentioned in Table 5. Poly isobutylene alt maleic anhydride (PMA) coated NPs (5 µg/ml) and untreated cultures were also included as controls.

The efficient retention of polymer functionalized NPs in cancer cells with the help of EPR effect and leaky vasculature system (pore diameter = 100 nm to 2 µm) [52, 53] reduces their non-specific biological interactions with plasma proteins, contributing towards higher bioavailability [52, 54]. SRB screening results for HepG2 and HT144 (Fig. 3a) cells showed strong cytotoxic effect (% viability < 50% approx.) upon treatment with drug loaded NPs compared to NTC. This cytotoxic effect was prominent when compared to free drug controls where cell viability was upto 70 - 80% approx. indicating higher bioavailability and better internalization of anticancer drugs when loaded on ferrite NPs.

Treated cells also exhibited morphological alterations such as cellular shrinkage and elongation which may affect their ability to metastasize (adhesion, migration and cellular invasion) [55]. PMA coated NPs showed upto 80% approx. viability indicating excellent biocompatibility of amphiphilic polymer at lower dose *in vitro*.

2.4 IC$_{50}$ concentrations of functionalized MFe$_2$O$_4$ NPs in cancer cells

MTT assay was performed to determine IC$_{50}$ concentrations of drug loaded NPs and their effect on metabolic activity of HepG2 and HT144 cells. Cells were exposed to several concentrations (1, 10, 25, 50 and 100 µg/ml) of NPs+Drugs and NPs-PMA for 24 hours. NTC and free drugs (DOX & MTX = 10 µM each) were included as controls. Percentage viabilities were plotted at all doses (Fig. 3b) and IC$_{50}$ values were determined (Table 7). In both cell lines, drug functionalized NPs caused almost 45 − 50% reduction in cellular viability at 1 µg/ml concentration which increased at higher doses.

In HepG2, cellular viabilities at 1 µg/ml dose ranged from 53.72 ± 5.65% to 56.40 ± 5.46% (p<0.001) for NPs+DOX and 50.30 ± 4.94 to 54.51 ± 4.24% (p<0.05) for MTX loaded NPs. ZFO NPs were most cytotoxic (IC$_{50}$ = 2.34 µg/ml and 1.08 µg/ml for ZFO+DOX and ZFO+MTX, respectively). In HT144 cells, cellular viabilities of 49.70 ± 1.41 to 52.10 ± 1.45% and 49.40 ± 3.53 to 50.29 ± 3.21 (p<0.0001) were observed upon treatment with NPs+DOX and NPs+MTX (1 µg/ml), respectively. NFO+DOX (IC$_{50}$ = 0.86 µg/ml) and CFO+MTX (IC$_{50}$ = 0.81 µg/ml) were most cytotoxic.

PMA coated NPs used as control in the study were comparatively non-toxic to the cells with relative % viability ranging from 98.53 ± 0.76 to 84.11 ± 1.29 against HepG2 using different NPs-PMA at various concentrations. Similarly, for HT144, % viability ranged from 96.35 ± 0.50 to 80.4 ± 2.48, indicating biocompatibility and higher tolerance of the drug free particles.

The drug loaded NPs showed 1.6 to 12 folds stronger effects when compared to the NPs-PMA at the same doses.

Table 7: IC$_{50}$ values (μg/ml) of drug loaded MFe$_2$O$_4$ nanoparticles with attached drug (μM)

Sample	HepG2		HT144		Lymphocytes	
	IC$_{50}$ (μg/ml)	Attached drug (μM)	IC$_{50}$ (μg/ml)	Attached drug (μM)	IC$_{50}$ (μg/ml)	Attached drug (μM)
FeO+DOX	2.48	0.04	2.18	0.03	22.68	0.36
CFO+DOX	3.81	0.16	2.08	0.09	35.96	1.51
NFO+DOX	3.97	0.07	0.86	0.01	18.35	0.32
ZFO+DOX	2.34	0.07	1.30	0.02	24.54	0.73
FeO+MTX	2.18	0.03	1.18	0.01	41.65	0.57
CFO+MTX	1.23	0.05	0.81	0.03	43.04	1.75
NFO+MTX	2.31	0.02	1.09	0.02	21.04	0.18
ZFO+MTX	1.08	0.02	1.02	0.02	38.71	0.71
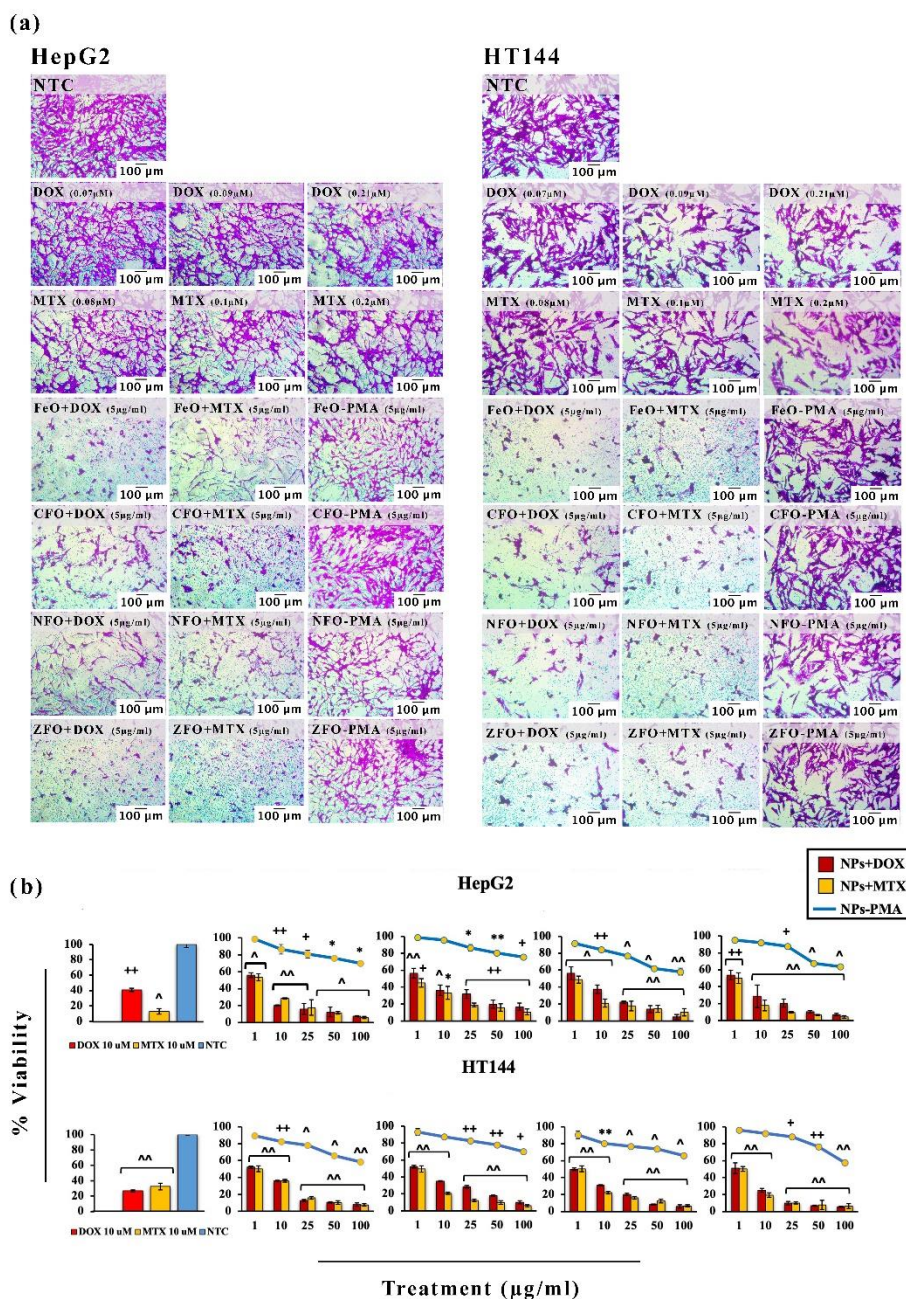
Figure 3: (a) Microscopic images of HepG2 and HT144 cells indicating cytotoxic potential of drug loaded (DOX and MTX) MFe₂O₄ (M = Fe, Co, Ni, Zn) NPs at 5 µg/ml dose, after 24 hour treatment. For comparison, free drug controls were included which represented total drug attached with NPs at said dose (DOX = 0.08, 0.21, 0.09, 0.09 µM; MTX = 0.08, 0.2, 0.1, 0.1 µM respectively). Untreated samples (NTC) and poly iso butylene alt maleic anhydride (PMA) coated samples (NPs-PMA) were also included as controls (5 µg/ml). Magnification = 200X, Scale bar = 100 µM. **(b)** Dose dependent cytotoxicity of drug functionalized MFe₂O₄ NPs in HepG2 and HT144 cells when treated with varying concentrations of NPs+Drugs (DOX and MTX) and NPs-PMA (1, 10, 25, 50 and 100 µg/ml) for 24 hours. (**Left to right**) Controls, FeO, CFO, NFO and ZFO. Controls included free DOX and MTX (10 µM each) and untreated cells (NTC) respectively. Plotted data indicates mean ± SD of independent triplicates. [*]p<0.05,

2.5 Functionalized MFe$_2$O$_4$ NPs cause apoptosis in dose dependent manner

Fractions of live, dead, and apoptotic cells (HepG2 and HT144) were determined quantitatively by fluorescent microscopy using AOPI staining. Cells were treated with drug loaded NPs for 3 hours at 5 and 10 µg/ml concentrations. NTC, NPs-PMA (10 µg/ml) and free drugs (DOX & MTX = 5 µM each) were included as controls. After treatment and staining with AOPI, cells were observed under fluorescent microscope where viable cells appeared green, apoptotic cells appeared orangish yellow and necrotic cells appeared red in color (Fig. 4a). Percent fractions of live, necrotic and apoptotic cells were calculated in each replicate and compared to NTC (Fig. 4b).

All drug loaded samples exhibited dose dependent response. Among DOX loaded NPs, ZFO+DOX was most cytotoxic in HepG2 cells with apoptotic cell fraction of 43.12 ± 2.35% at 5 µg/ml dose (p<0.01). Whereas FeO+DOX, CFO+DOX and NFO+DOX showed 39 ± 3.39%, 32.83 ± 3.81 and 29.5 ± 1.93% apoptotic cells (p<0.05) respectively. Percent apoptotic cells increased by 1.4 – 2.5 folds (p<0.05) at higher dose with maximum apoptosis observed in ZFO+DOX (91.24 ± 5.43%). In case of MTX loaded samples, about 40.51 ± 3.70% to 56.26 ± 5.34% apoptotic cells (p<0.05) were observed at 5 µg/ml dose with ZFO+MTX being most cytotoxic. Apoptotic fraction increased up to 2 folds in the presence of CFO+MTX, NFO+MTX and ZFO+MTX at 10 µg/ml dose (p<0.01). Whereas FeO+MTX exhibited 9 folds increase in necrotic cells (p<0.005). Free drugs (DOX and MTX; 5 µM each) used as controls resulted in 33.07 ± 3.72% and 36.25 ± 3.23% apoptotic cells (p<0.01) respectively.

In HT144 cells, 42.15 ± 3.45 to 63.62 ± 3.51% apoptotic cells (p<0.05) were observed in the presence of DOX loaded NPs (5 µg/ml) with highest apoptotic fraction of 63.66 ± 3.5% upon

NFO+DOX treatment. An increase in apoptotic cells up to 1.3 and 1.7 folds (p<0.01) was observed in CFO and FeO+DOX respectively at 10 µg/ml dose. Whereas significantly (p<0.01) high cell death (9.6 - 14 fold increase in necrotic cells) was observed in ZFO and NFO+DOX nanocarriers respectively. In the presence of MTX loaded NPs, CFO and ZFO showed maximum apoptotic cells i.e., 66.57 ± 1.39 and 60.52 ± 3.81% respectively (p<0.005) at 5 µg/ml concentration. At higher dose, percent apoptotic cells increased up to 1.5 folds in FeO, CFO and NFO+MTX (p<0.005). ZFO+MTX however, caused maximum cell death with 12X increase in necrotic cells. DOX and MTX controls caused 68.05 ± 5.55 and 59.13 ± 3.93% apoptosis respectively (p<0.001).

In both cell lines, PMA coated NPs showed higher cellular viability after 3 hours treatment at 10 µg/ml dose (HepG2 = 82.22 ± 5.92 to 94.74 ± 2.03; HT144 = 93.36 ± 5.11 to 95.91 ± 5.73), indicating biocompatibility of NPs-PMA at said dose and treatment time.
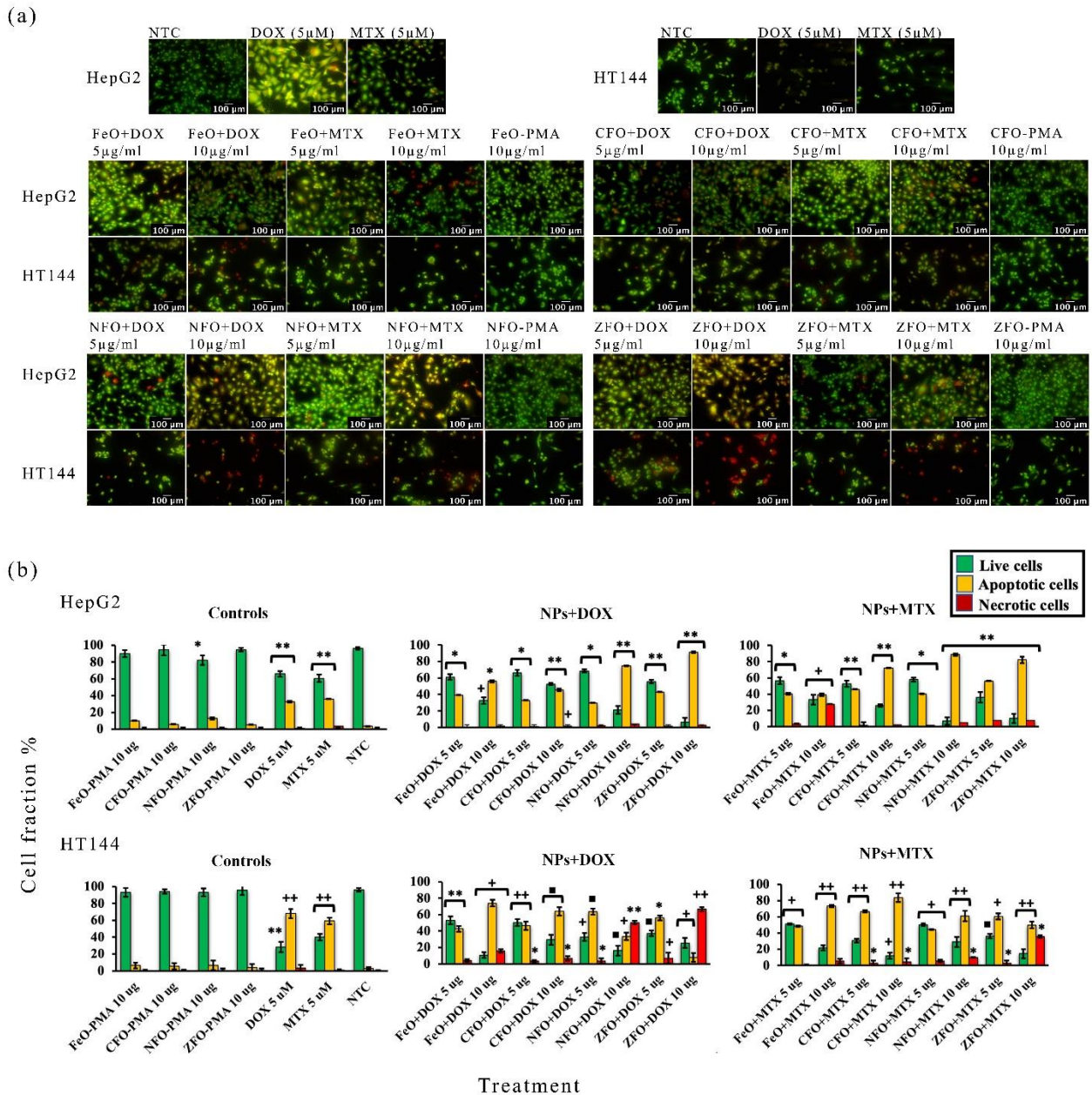
Figure 4: (a) Fluorescent microscopic images of HepG2 and HT144 cells upon treatment with drug loaded (DOX and MTX) MFe$_2$O$_4$ (M = Fe, Co, Ni, Zn) NPs at 5 and 10 μg/ml doses for 3 hours. Controls included free drugs (DOX and MTX) at 5 μM concentration, NPs-PMA (10 μg/ml) and untreated cells (NTC). Live cells emit green, necrotic cells red and apoptotic cells emit yellow to orange fluorescence due to AOPI staining. Magnification = 200X, Scale bar = 100 μM. **(b)** Quantitative analysis of percent viable, apoptotic, and necrotic cellular fractions (mean ± SD of experimental triplicates) in HepG2 and HT144 cells with controls. *p<0.05, **p<0.01, +p<0.005, ++p<0.001 and ˙p<0.0005 (two tailed t-test when samples were compared to NTC).

2.6 Cells undergo oxidative stress upon treatment with functionalized MFe$_2$O$_4$ NPs

Generation of ROS has been associated with DNA damage, inflammation, apoptosis and senescence in cells [56]. H$_2$-DCFDA assay was used to determine cellular ROS production in HepG2 and HT144 cells upon treatment with NPs over a period of time. Cells were exposed to NPs+DOX and NPs+MTX at IC$_{50}$ concentrations and increase in fluorescence was determined relative to untreated control (NTC) over a time interval (0 - 45 minutes). Several studies have indicated that spinel ferrite MFe$_2$O$_4$ (M = Fe, Co, Ni, Zn) NPs cause cytotoxicity via oxidative stress which results in damage to cell membrane, proteins and DNA [56-58]. However, how NPs are processed inside the cell, is also a contributing factor in ROS production [59]. For example, metallic NPs transported to lysosomes produce more ROS due to enhanced acidic degradation as compared to cytosol [60]. Besides, intrinsic antioxidant potential of various cells also contribute towards biocompatibility and extent of ROS generation via metallic NPs [61, 62].

In the present work, free DOX and MTX produced non-significant ROS in both cell lines which enhanced significantly upon NP mediated drug delivery. An increase in ROS production was observed in first 5 minutes of treatment which elevated steadily over the period of time. NPs+DOX produced significant ROS ($p<0.05$) in HepG2 cells (Fig. 5a) after treatment for 35 - 45 minutes. Whereas NPs+MTX showed significant ($p<0.05$) results at 20 - 45 minutes of exposure. Drug loaded NPs exhibited 1.6 to 2 folds enhanced ROS production in HepG2 cells compared to free drug controls. HT144 cells however, were more susceptible to oxidative damage via NPs+drugs and free drug controls compared to HepG2 cells. Both NPs+DOX and NPs+MTX started producing significant ($p<0.05$) ROS at 5 minutes exposure time with 2 to 3 folds increased effect compared to free drug controls. Lower sensitivity of HepG2 cells towards

oxidative stress can be attributed to the presence of xenobiotic detoxification and antioxidant mechanisms [62, 63].

2.7 Functionalized MFe₂O₄ NPs cause cell cycle arrest in cancer cells

Evidence of oxidative damage in treated cells may indicate DNA damage and possible effects on cell cycle progression causing damaged cells to accumulate in subG1, G1, S or G2/M phases of cell cycle [64]. To determine effects of drug loaded MFe_2O_4 NPs on cell cycle progression, HepG2 and HT144 cells, treated with NPs at IC_{50} doses were analyzed by flow cytometry. Data obtained from each sample was compared to NTC (Fig. 5b).

In HepG2 cells, all NPs+DOX, FeO+MTX and CFO+MTX showed a significant ($p<0.005$) G1 arrest resulting in a decreased cellular population in S and G2/M phases ($p<0.05$). Similar observations were made in free DOX (0.2 µM) control, which was consistent with a previous report [65]. In contrast, NFO+MTX and ZFO+MTX exhibited delay in S phase ($p<0.005$) causing inhibition of cellular replication and progression towards G2/M. Furthermore, a significant ($p<0.05$) G2/M phase arrest in FeO+MTX and ZFO+MTX was also observed. Free MTX (0.2 µM) control produced G1 and S phase arrest ($p<0.005$) with reduced cells in G2/M phase ($p<0.05$). Methotrexate has been reported previously to cause cytotoxicity in S phase and stop progression of G1 to S phase [66].

In HT144 cells, all DOX loaded NPs showed non-significant S phase arrest except FeO+DOX which caused G1 arrest. CFO+DOX and ZFO+DOX were also responsible for G2/M arrest ($p<0.01$) accompanied by lower cell population at G1. Comparably, free DOX control also produced G2/M arrest ($p<0.01$) and reduced number of cells in G1 phase ($p<0.01$). All MTX loaded NPs and free MTX control caused G2/M arrest ($p<0.01$) in cells with non-significant S phase arrest, lowering cellular population in G1 phase ($p<0.01$).

Obtained flow cytometry results from drug loaded NPs were comparable to free drug controls (0.2 µM). However, considering that the amount of drug attached with IC_{50} doses of NPs was much lower than 0.2 µM (as mentioned in Table 7), it was speculated that nanocarriers amplified the effects due to improved and efficient drug delivery at a much lower dose compared to free drug controls.
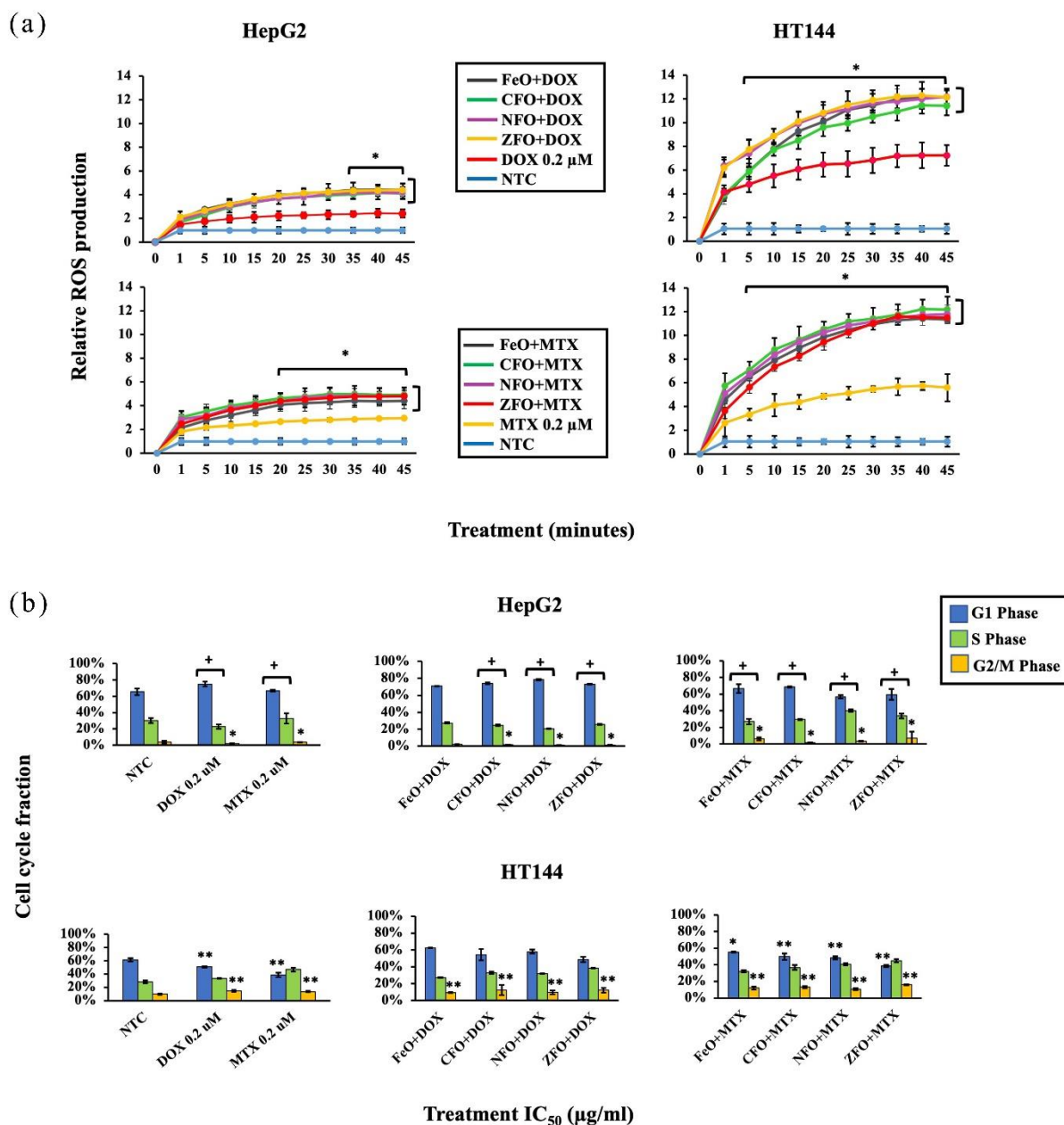
Figure 5: (a) Intracellular ROS generation in HepG2 and HT144 cells upon treatment with drug loaded (DOX and MTX) MFe_2O_4 (M = Fe, Co, Ni, Zn) NPs for 0 - 45 minutes at IC_{50}

doses. Free drugs (DOX and MTX = 0.2 μM each) and untreated cells (NTC) were included as controls. ROS generation in cells was determined relative to NTC. Data represented as mean ± SD of experimental triplicates. *p<0.05 (paired two tailed t-test when compared to NTC). **(b)** Effect of drug loaded MFe_2O_4 NPs on cell cycle progression in HepG2 and HT144 cells determined by flow cytometry. Cells were exposed to IC_{50} doses of NPs for 24 hours. Untreated cells (NTC) and free drugs (DOX and MTX = 0.2 μM) were included as controls. *p<0.05, **p<0.01, $^+$p<0.005 (paired two tailed t-test when compared to NTC).

2.8 Functionalized MFe_2O_4 NPs cause genotoxicity in treated cells

Alkaline comet assay was performed to determine genotoxicity of drug loaded NPs in HepG2 and HT144 cells (Fig. 6a). The olive tail moment was measured for each sample and relative calculation with respect to NTC was performed as a measure of DNA damage (Fig. 6b). Genotoxic effect of NPs may arise from their direct interaction with DNA or enhanced ROS production by cellular components. If unrepaired or misrepaired, these lesions may contribute towards replication errors, and gene or chromosomal alterations [67].

Genotoxicity of spinel ferrite NPs has been reported earlier [68, 69]. However, other factors such as NP size and ligand used for functionalization may contribute towards genotoxic activity. Smaller NPs (< 50 nm) have large surface area which increases their biological interactions and hence genotoxic potential [70]. Polymeric coatings, on the other hand, are aimed at enhancement of colloidal stability and facilitation of NPs interaction with plasma membrane associated proteins [71]. In addition, charge of polymeric coatings also governs NPs uptake by cells. Positively charged polymers have been reported to enhance genotoxicity due to better internalization of NPs via plasma membrane (electrostatic interaction) and direct interaction with nucleus and DNA. Whereas, negatively charged coating such as PMA has no effect on genotoxicity [72].

In HepG2 cells, FeO+DOX and CFO+DOX showed maximum genotoxicity with relative tail moments of 6.41 ± 1.75 and 4.68 ± 2.45 (p<0.01) respectively which were higher (up to 2 folds)

than free DOX control (2.77 ± 2.35; p<0.05). Among MTX nanocarriers, CFO+MTX and ZFO+MTX were highly genotoxic (p<0.005) having relative tail moments of 4.58 ± 4.23 and 4.21 ± 4.93 respectively. Results were up to 1.6 folds higher than that of free MTX control (2.82 ± 3.24; p<0.01).

In HT144 cells, maximum genotoxicity (p<0.005) was observed in CFO+DOX and ZFO+DOX with relative tail moments of 6.72 ± 1.44 and 5.44 ± 1.06 respectively. Results were enhanced up to 2.4 folds compared to free DOX, where relative tail moment of 2.78 ± 1.66 (p<0.01) was observed. Relative tail moments in CFO+MTX and ZFO+MTX were 3.98 ± 1.09 and 4.44 ± 0.88 (p<0.005), respectively which were almost 2 folds higher than free MTX control (2.22 ± 1.21; p<0.05). Obtained results were therefore indicative of enhanced genotoxic behavior in cancer cells upon NP mediated drug delivery.

2.9 Functionalized MFe$_2$O$_4$ NPs cause DNA fragmentation in treated cells

Both HepG2 and HT144 cells showed apoptotic DNA fragmentation (Fig. 6c), upon treatment with drug loaded NPs at IC$_{50}$ doses for 24 hours. Distinct bands of 180 bp were visualized on 2% agarose indicating shearing of DNA as a result of apoptosis in treated cells. These findings indicated that drug loaded NPs cause cytotoxicity in cancer cells via oxidative stress leading to apoptosis and DNA fragmentation.

2.10 Functionalized MFe$_2$O$_4$ NPs alter Ki-67 and p53 expression in treated cells

p53 is a tumor suppressor protein also known as 'guardian of the genome'. It is involved in downstream regulation of genes involved in apoptosis, DNA repair and cell cycle arrest. Overexpression of p53 is triggered by stress stimuli such as hypoxia, ROS, ionizing radiations, and carcinogens. Normal cells have low expression of p53 but its half-life may increases upto several hours under stress, resulting in elevated expression [73, 74]. Enhanced expression of

p53 in response to cellular stress has been associated with cell cycle regulation. It causes G1 arrest by inhibiting cyclin D and stimulating p21 expression. It is also involved in repairing lethal DNA damages (double stranded breaks) via Gadd45, by arresting cells at G1. G2 arrest occurs by p53 mediated reduction in cyclin B1 and S phase arrest happens by regulation of mitotic spindle checkpoints. Extensive DNA damage however, leads to apoptosis [75].

Whereas, Ki-67 is an important proliferative and prognostic cancer biomarker, expressed in nucleus during cell cycle. It is important for cell division and biosynthesis of ribosomal RNA, expressed variably throughout the cell cycle (high in G2/M phase and low in G1 and S phase). High expression of Ki-67 usually contributes to poor survival rates in cancer patients [76].

In this study, effect of drug loaded MFe_2O_4 (M = Fe, Co, Ni, Zn) NPs treatment (IC_{50} doses) on cancer biomarker expression was evaluated via ICC (Fig. 6d). Untreated cells (NTC) exhibit high expression of Ki-67 (HepG2 = $79.62 \pm 3.72\%$; HT144 = $75.67 \pm 6.14\%$), indicating high proliferative potential of cancer cells and expression of p53 was relatively low (HepG2 = $39.23 \pm 2.91\%$; HT144 = $26.44 \pm 1.25\%$) (Fig. 6e).

Upon treatment p53 expression was elevated, potentially responsible for cell cycle arrest and apoptosis. In HepG2 cells, DOX loaded CFO and ZFO nanocarriers showed maximum p53 expression of 70.43 ± 4.82 and $79.47 \pm 3.65\%$ (p<0.001), respectively. Similar results were observed in MTX loaded NPs where maximum p53 expression of 79.13 ± 5.61 and $73.65 \pm 2.93\%$ (p<0.0005) was observed in CFO+MTX and ZFO+MTX respectively. An increase in expression was observed when compared to free drug controls where only $54.61 \pm 1.32\%$ and $65.33 \pm 1.71\%$ p53 expression was observed in DOX and MTX respectively (p<0.005). On the other hand, a decrease in Ki-67 expression was observed in treated cells indicating potential role in inhibition of cellular proliferation. Significantly stronger (p<0.005) decrease in Ki-67 expression was observed in CFO and ZFO nanocarriers (CFO+DOX = $36.9 \pm 1.57\%$,

ZFO+DOX = 38.1 ± 1.17%, CFO+MTX = 56.3 ± 5.23% and ZFO+MTX = 66.9 ± 5.55%).

Free drug controls however reduced Ki-67 expression by 12% approx. (DOX = 66.6 ± 5.82%,

MTX = 69.2 ± 5.14%) compared to NTC.

Similar observations were made in HT144 cells where CFO and ZFO nanocarriers were highly

effective. Among DOX nanocarriers, CFO+DOX showed maximum p53 expression of 67.66

± 4.66% ($p < 0.0005$) and lowest Ki-67 expression of 37.75 ± 5.31% ($p < 0.001$). Whereas p53

and Ki-67 levels were 46.63 ± 1.65% ($p < 0.005$) and 58.27 ± 4.86% ($p < 0.01$) in free DOX

control. Amidst MTX nanocarriers, Ki-67 levels of 64.44 ± 4.62% and 64.15 ± 5.21% were

observed in CFO+MTX and ZFO+MTX, respectively. Both nanocarriers also elevated p53

expression upto 75% ($p < 0.001$). Free MTX however, showed Ki-67 and p53 levels of 71.82 ±

3.11% ($p < 0.01$) and 67.66 ± 4.68% ($p < 0.001$), respectively indicating better performance of

drug loaded NPs. Obtained results also suggested a stronger inhibition of Ki-67 by DOX loaded

NPs as compared to NP+MTX in both cell lines.

In both cell lines, a decrease in Ki-67 expression may indicate low proliferative potential of

cancer cells after treatment with nanocarriers. But, variable expression of Ki-67 during cell

cycle may also affect these findings [77]. Flow cytometric results revealed that NPs+DOX

caused G1 and S phase arrest in HepG2 and HT144 cells respectively which may result in

relatively low expression of Ki-67 in these treatment groups and comparatively higher

expression in samples showing G2/M arrest in cell cycle. Furthermore, irreparable DNA

damage (double stranded breaks) also contributes towards irreversible G1 arrest and

senescence which decreases the proliferative capacity of the cell [78]. Since the effect of Ki-

67 on cell survival and proliferation has not been understood clearly [76], it is therefore not

possible to elucidate effect of certain therapeutic interventions on this biological event without

extensive investigations.
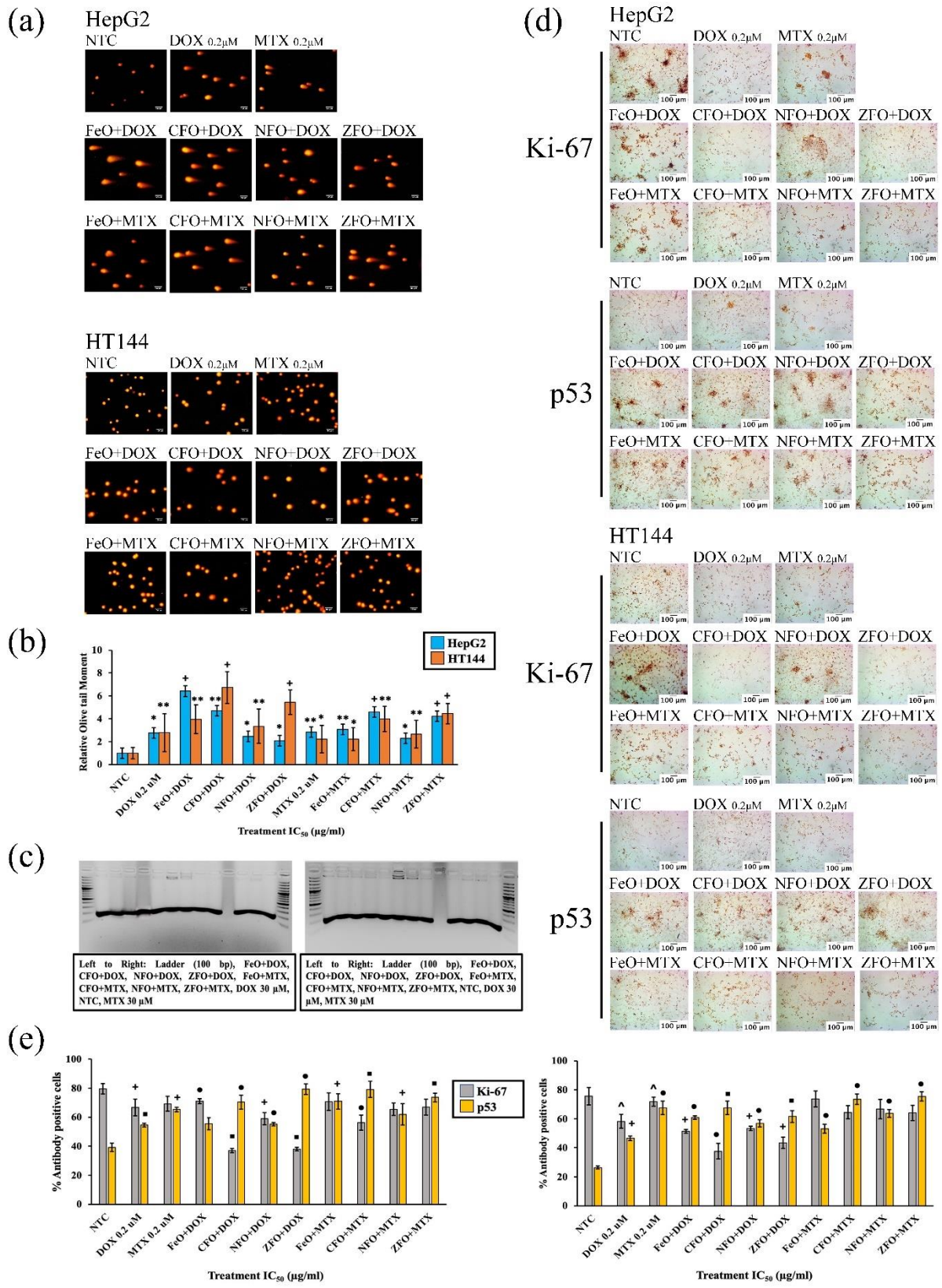
Figure 6: (a) Comet images of HepG2 and HT144 cells upon treatment with drug loaded (DOX and MTX) MFe₂O₄ (M = Fe, Co, Ni, Zn) NPs at IC₅₀ doses for 1 hour. Controls included free

drugs (DOX and MTX) at 0.2 μM concentration and untreated cells (NTC). Cells were stained with propidium iodide (5 µg/ml). Magnification = 200X, Scale bar = 100 μM. **(b)** Olive tail moments as measure of DNA damage (mean ± SD) were calculated relative to NTC for each sample. $^*p<0.05$, $^{**}p<0.01$ and $^+p<0.005$ (paired two-tailed t-test when compared to NTC). **(c: left to right)** Apoptotic DNA fragmentation in HepG2 and HT144 cells after treatment with drug loaded (DOX and MTX) MFe_2O_4 NPs for 24 hours at IC_{50} doses. Free drugs (DOX and MTX = 30 μM) and untreated cells (NTC) were included as controls. DNA samples were electrophoresed on 2% agarose gel for 2 hours at 50 V along with DNA ladder (100 bp). **(d)** Microscopic images of Immunocytochemical (ICC) staining of HepG2 and HT144 cells with Ki-67 and p53 mouse monoclonal antibodies after treatment with IC_{50} doses of drug loaded (DOX and MTX) MFe_2O_4 NPs for 24 hours. Controls included untreated cells (NTC) and free drugs (DOX and MTX = 0.2 μM). Magnification = 200X, Scale bar = 100 μM. **(e: left to right)** Bar charts represent expression levels of Ki-67 and p53 antibodies in treated HepG2 and HT144 cells respectively. Antibody positive cells were counted in treated and untreated samples and percentages were calculated (mean ± SD). $^\wedge p<0.01$, $^\bullet p<0.001$, $^+p<0.005$ and $^\bullet p<0.0005$ (paired two-tailed t test upon comparison with NTC)

2.11 Functionalized MFe_2O_4 NPs reduce cellular viability in HepG2 and HT144 3D spheroid models

The use of three-dimensional (3D) spheroid models for high-throughput drug screening *in vitro* is favored due to their close resemblance to *in vivo* tumors. Moreover, they possess several tumor hallmarks such as hypoxia, cellular interaction, drug resistance and dense extracellular matrix, allowing better pathobiological studies of human cancers [79].

Here, spheroids of HepG2 and HT144 cells were grown for cytotoxicity assessment of drug functionalized MFe_2O_4 NPs (5 µg/ml). Obtained HepG2 and HT144 spheroids had average diameters of 420 ± 21.5 and 582 ± 72 µm respectively which reached maximum at 14th day (HepG2 = 450 ± 16.33 and HT144 = 713 ± 81.3 µm). HepG2 formed compactly packed spheroids whereas, HT144 spheroids were loosely bound (Fig. 7).

In HepG2 spheroids, slight reduction in spheroid diameter was observed after treatment with drug loaded NPs. Spheroids were also not highly disintegrated (Fig. 7). ZFO+DOX and CFO+MTX among DOX and MTX nanocarriers, caused maximum reduction (p<0.005) in spheroid diameter upto 20 µm (Fig. 8a) at 14th day. Slight disintegration of spheroids was also

observed at 7th and 14th day of treatment. Whereas, free DOX and MTX reduced diameter upto 30 µm (p<0.005) without prominent spheroid integration. Cellular viability determined via trypan blue assay at 14th day indicated upto $57 \pm 3.1\%$ (p<0.01) cell death in treated spheroids compared to $37.5 \pm 2.3\%$ and 39.8 ± 1.5 in free DOX and MTX controls respectively (Fig. 8b). In HT144 spheroids, CFO+DOX and ZFO+MTX among DOX and MTX nanocarriers, produced maximum significant reduction in spheroid diameter (Fig. 8a) at 14th day (423 µm, p<0.005 and 168 µm, p<0.0005 respectively) with 74 ± 8.9 and $81 \pm 5.3\%$ (p<0.01) cellular death (Fig. 8b). Cells lost their compactness and started to disaggregate after 3 days of treatment which increased with the passage of time (Fig. 7). Average reduction in diameter of spheroids after treatment with free DOX and MTX samples was 350 and 387 µm (p<0.01) with 43 ± 2.3 and $39.7 \pm 5.6\%$ (p<0.01) cell death respectively. Obtained results suggested better internalization of drug loaded NPs compared to free drugs.

2.12 Functionalized MFe_2O_4 NPs cause inhibition of MDR pump activity in treated HepG2 and HT144 cells

Due to overexpression of P-glycoprotein (P-gp), cancer cells possess the ability to efflux chemotherapeutic drugs, a phenomenon known as called MDR. P-gp belongs to ABCB1 family of ABC proteins and is involved in efflux of doxorubicin, paclitaxel, vincristine, rhodamine and etoposide [80]. Whereas MRP1 is a member of ABCC1 family, responsible for efflux of xenobiotics and hydrophobic drugs namely methotrexate, vinca-alkaloids, anthracyclines, antiandrogens, and heavy metals. Both MDR1 and MRP1 proteins are majorly responsible for lowering therapeutic outcomes of chemotherapy [81].

Present study was conducted to evaluate role of drug functionalized MFe_2O_4 NPs in hindering MDR pump activity in HepG2 and HT144 cells after 24 hours treatment at IC_{50} doses. Retention of fluorometric dye was estimated relative to NTC (Fig. 8c). Among DOX

nanocarriers in HepG2, CFO+DOX and ZFO+DOX produced maximum significant inhibition of MDR pump, with upto 6.8X ($p < 0.005$) dye retention compared to NTC. Similarly, among MTX nanocarriers, highest dye retention upto 4X was observed in CFO+MTX and ZFO+MTX ($p < 0.05$). Dye retention in free DOX and MTX was lower (3X and 1.9X respectively). Cyc A used as positive control, caused inhibition of MDR upto 4 folds.

Similar results were obtained in HT144 cells. Among DOX nanocarriers, CFO+DOX and ZFO+DOX were responsible for maximum significant inhibition of MDR pump (upto 7 folds, $p < 0.005$). Whereas dye retention in free DOX was 3.9 folds compared to NTC. Amidst MTX nanocarriers, ZFO+MTX and CFO+MTX proved to be most efficient with upto 6.5X ($p < 0.01$) dye retention compared to free MTX with lower dye retention of 4.1 folds.

The results indicated possible role of drug loaded CFO and ZFO NPs in combating MDR in cancer cells.
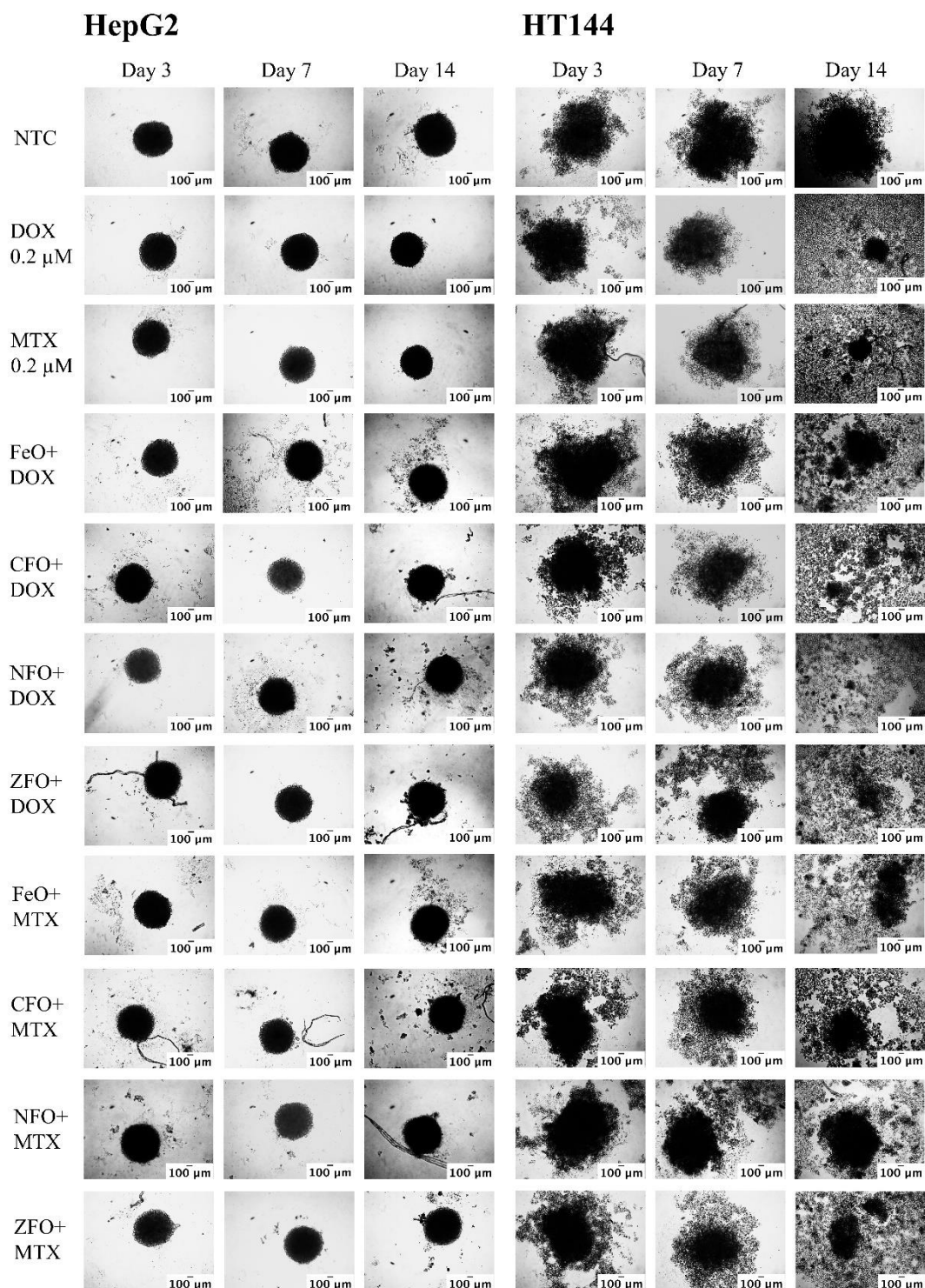
Figure 7: Microscopic images (Magnification = 100X, Scale bar = 100 µm) of 3D spheroids of HepG2 and HT144 cells. Spheroids were allowed to grow for 3 days and then treated with drug loaded (DOX and MTX) MFe_2O_4 (M = Fe, Co, Ni, Zn) NPs at 5 µg/ml for 14 days. Controls included free drugs (DOX and MTX = 0.2 µM each) and NTC. Media was replenished

after regular intervals and photographs were taken after 3, 7 and 14 days to observe changes in spheroid morphology.
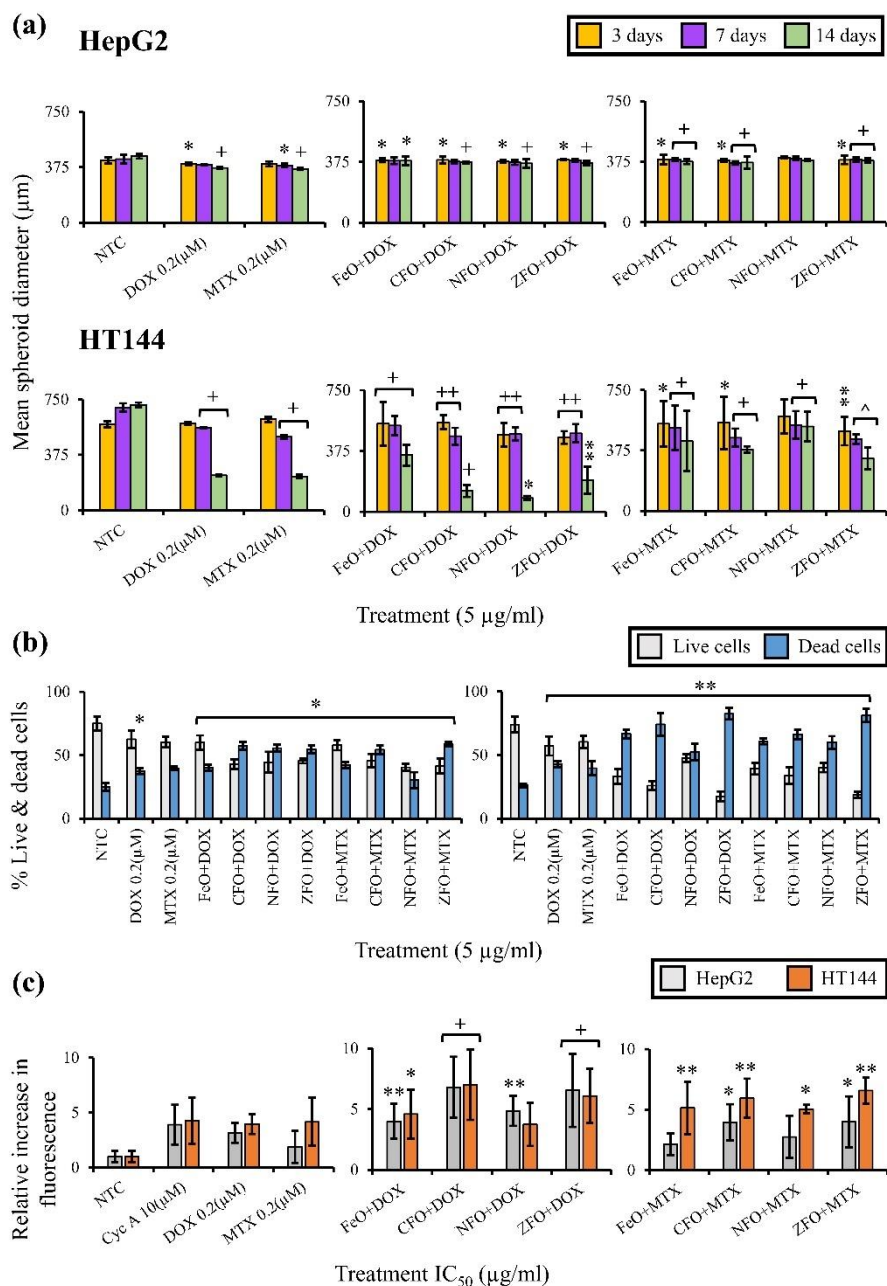
Figure 8: (a) Bar charts indicating changes in HepG2 and HT144 3D spheroids diameter upon exposure to drug loaded (DOX and MTX) MFe_2O_4 (M = Fe, Co, Ni, Zn) NPs at 5 µg/ml dose, after 3, 7 and 14 days. Controls included free drugs (DOX and MTX = 0.2 µM each) and NTC. After each time point average spheroid diameter was calculated by ImageJ software. Plotted data indicates mean ± SD of multiple readings covering maximum and minimum diameter ranges of spheroids. **(b: left to right)** Bar charts indicating percentage viability and death in treated HepG2 and HT144 3D spheroids after 14 days. Live and dead cells in each sample were counted using trypan blue assay. Data plotted indicates mean ± SD of three replicates. *p<0.05, **p<0.01, +p<0.005, ++p<0.001 and ^p<0.0005 (paired two-tailed t test when compared to NTC). **(c)** Bar charts representing MDR pump inhibition (mean ± SD) in HepG2 and HT144 cells

34

treated with IC$_{50}$ doses of drug loaded (DOX and MTX) MFe$_2$O$_4$ NPs for 24 hours. Controls included NTC, free drugs (DOX and MTX = 0.2 µM each) and MDR inhibitor cyclosporin A (Cyc A = 10 µM). Inhibition of MDR pump activity was determined by increase in fluorescence relative to NTC. *p<0.05, **p<0.01 and $^+$p<0.005 (paired two-tailed t test when samples were compared to free drug controls).

2.13 Functionalized MFe$_2$O$_4$ NPs showed higher IC$_{50}$ in normal cells as compared to cancer cells

Cytotoxicity of drug loaded NPs was assessed in fresh human lymphocytes to determine their biocompatibility *in vitro* using MTT assay. Freshly collected lymphocytes were exposed to varying concentrations (1, 10, 25, 50 and 100 µg/ml) of drug loaded NPs for 24 hours. Untreated cells (NTC) and free drug controls (DOX and MTX) at 0.04, 0.4, 1, 2 and 4 µM concentrations (equivalent to drug attached with tested concentrations of NPs) were also included as controls.

Results indicated highest cytotoxicity of drug loaded NFO NPs in dose dependent manner with % viability values (highest to lowest) ranging from 75.37 ± 2.41 to 8.52 ± 4.75 in NFO+DOX and 85.56 ± 3.12 to 17.52 ± 9.46 in NFO+MTX. All NPs+DOX were significantly cytotoxic (p<0.05) at 25 µg/ml and higher concentrations (p<0.05) excluding NFO which was cytotoxic at 10 µg/ml as well (p<0.05). DOX loaded CFO and ZFO were least cytotoxic compared to other NPs with % viability values (highest to lowest) ranging from 83.93 ± 2.01 to 20.91 ± 6.42 for CFO and 81.56 ± 1.33 to 19.74 ± 5.91 for ZFO at all doses (Fig. 9b).

Among MTX loaded NPs, all samples were significantly cytotoxic at 50 µg/ml and higher concentrations (p<0.05). Whereas NFO was cytotoxic (p<0.005) even at 25 µg/ml. ZFO and CFO loaded with MTX were most biocompatible among all with % viabilities (highest to lowest) ranging from 88.67 ± 5.01 to 24.33 ± 3.92 and 87.81 ± 1.60 to 21.26 ± 3.94 respectively (Fig. 9c) at all tested doses. Free drug controls (DOX and MTX) showed significant cytotoxicity (p<0.05) at highest dose of 4 µM (Fig. 9a).

Obtained results suggested increased selectivity of nano-carriers towards cancer cells as previously reported [82] with approximately 10 - 35 times higher IC_{50} values (except NFO+DOX) in normal cells compared to cancer cells (Table 7).
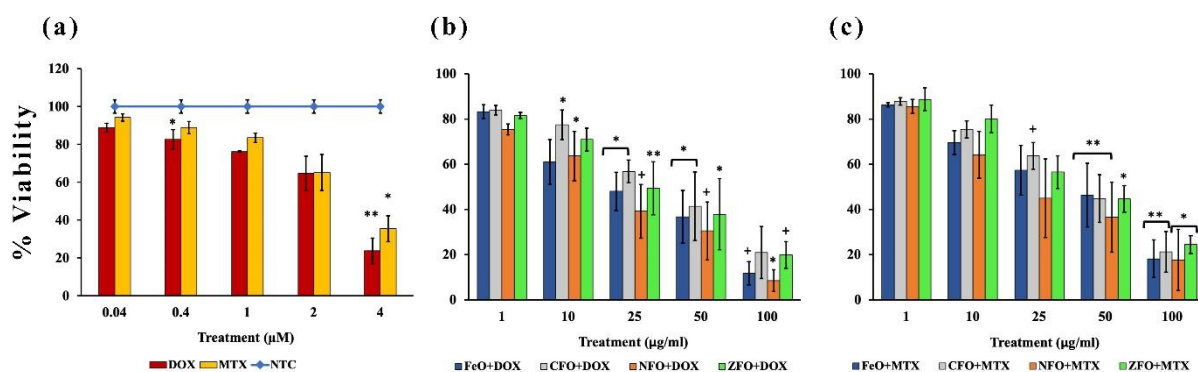
Figure 9: Dose dependent cytotoxicity of drug loaded (DOX and MTX) MFe_2O_4 (M = Fe, Co, Ni, Zn) NPs in fresh human lymphocytes. Cells were treated with varying concentrations of NPs (1, 10, 25, 50 and 100 µg/ml) for 24 hours. **(a)** Controls included DOX and MTX (0.04, 0.4, 1, 2 and 4 µM equivalent to drug attached with NPs at tested doses) and untreated cells (NTC). **(b)** Dose dependent cytotoxicity of DOX and **(c)** MTX loaded NPs in human lymphocytes. Plotted data indicates mean ± SD of three independent biological replicates with triplicates for all samples. $^*p<0.05$, $^{**}p<0.01$, $^+p<0.005$ (paired two tailed t-test when samples were compared to NTC).

3. Conclusion

The present research describes sono-chemically synthesized, biocompatible, highly colloidal, drug (DOX and MTX) functionalized MFe_2O_4 (M = Fe, Co, Ni, Zn) NPs for *in vitro* anticancer drug delivery. All nanocarriers showed significantly increased (p<0.005) drug release at acidic pH 5.5 compared to normal physiological pH 7.4, indicating their specificity towards cancer cells. *In vitro* cytotoxicity analysis indicated increased cytotoxicity in dose dependent manner compared to free drugs, with IC_{50} values ranging from 0.81 - 3.97 µg/ml in cancer cells and 18.35 - 43.04 µg/ml in normal cells. Similarly, cytotoxicity screening in 3D spheroids suggested better internalization of drug loaded NPs compared to free drugs. Most promising results were obtained in CFO and ZFO nanocarriers. Overall, NPs cause dose dependent

cytotoxicity via ROS generation causing genotoxicity, p53 mediated cell cycle arrest leading towards apoptosis. Furthermore, Ki-67 expression was highly inhibited ($p<0.005$) in the presence of CFO+DOX and ZFO+DOX nanocarriers, indicating their potential anti-proliferative capability in cancer cells. In addition, CFO and ZFO nanocarriers showed significant ($p<0.05$) inhibition of MDR pump activity in HepG2 and HT144 cells, suggesting their suitability for multidrug resistant cancers. Excellent colloidal stability, magnetic properties (coercivity = 883 and saturation magnetization = 56 emu/g), specificity towards cancer cells support CFO nanocarriers as promising candidates for targeted cancer therapy domains. However, further investigations regarding pathway analysis, *in vivo* cytotoxicity and magnetic field assisted drug delivery are needed.

4. Experimental

4.1 Materials

Iron nitrate [$Fe(NO_3)_3.9H_2O$], cobalt nitrate [$Co(NO_3)_2.6H_2O$] were purchased from UNI-Chem, zinc nitrate [$Zn(NO_3)_2.6H_2O$)], nickel nitrate [$Ni(NO_3)_2.6H_2O$], chloroform, oleic acid ($C_{18}H_{34}O_2$) were purchased from Applichem, poly (isobutylene-alt-maleic anhydride), dodecylamine, tetrahydrofuran (THF), 1-Ethyl-3-(3-dimethylaminopropyl) carbodiimide (EDC), doxorubicin (DOX), methotrexate (MTX), Tris/borate/EDTA (TBE) buffer, Dulbecco's Modified Eagle's Medium (DMEM), Rosewell Park Memorial Institute (RPMI-1640) medium, GPPS (2mM L-glutamine, 1mM Na-pyruvate, 100 U/ml penicillin, 100 ug/ml streptomycin), Triton X-100, trizma base, trypsin/EDTA, Sulforhodamine B (SRB), ethidium bromide, sodium dodecyl sulfate (SDS), 2',7'-dichlorodihydrofluorescein diacetate (H2-DCFDA) and 3-(4,5-Dimethylthiazol-2-yl)-2,5-diphenyltetrazolium bromide (MTT), propidium iodide (PI), acridine orange (AO), RNAse A and dimethyl sulfoxide (DMSO) were purchased from Sigma Aldrich (USA). DNA ladder (100 bp) and agarose (low melting and

37

normal) were purchased from Thermo Fischer Scientific and Hydra Gene Co., Ltd, respectively. Ethanol, trichloroacetic acid (TCA), trypan blue, fetal bovine serum (FBS), orange G, sodium hydroxide (NaOH) and Dibutylphthalate Polystyrene Xylene (DPX) mounting medium were purchased from Merck Germany. Antigen retrieval solution (K8004), Ki-67 (clone MIB-1), p53 (clone DO-7) mouse monoclonal anti-human antibodies, horseradish peroxidase (HRP) conjugated secondary antibody (DM822), peroxidase blocker (DM821), diaminobenzidine (DAB) + chromogen (DM827) and hematoxylin (K8018) were obtained from Agilent Technologies, Inc. (USA).

4.2 Colloidal synthesis of MFe_2O_4 (M = Fe, Co, Ni, Zn) NPs

The two-step sonochemical method was used for MFe_2O_4 (M = Fe, Co, Zn, Ni) NPs synthesis. Coprecipitation method was used in the first step for 0.2 M synthesis of MFe_2O_4 nanoparticles by mixing iron nitrate [Fe $(NO_3)_3.9H_2O$] and (Co/Zn/Ni) nitrates with molar ratio Fe: M (2:1) in 100 ml deionized water. The solution was stirred for 15 minutes, heated at $70^\circ C$ and further stirred for an hour after adding 3M NaOH that settled down formed precipitates. The precipitates were washed four times and collected with the help of a magnet. Samples were dried in the oven and annealed at $600^\circ C$ and redispersed in oleic acid (1:3) using sonication for 4 hours. The resultant precipitates were washed with methanol and resuspended in chloroform [43].

4.3 Physical characterizations

Structural studies were carried out by X-ray diffraction (XRD) D8-Advance Bruker AXS diffractometer with CuKα radiation (λ = 1.54 Å). The Debye Scherrer formula (Equation 1) was used to calculate average crystallite size of NPs from the XRD peak of the (311) plane [43]:

$$D = {K\lambda}/{\beta Cos\theta} \quad \cdots\cdots\cdots\cdots\cdots\cdots\cdots\cdots\cdots\cdots\cdots\cdots\cdots\cdots \quad (1)$$

Where D is average crystallite size, K = 0.94 and $\lambda = 1.54\,\text{Å}$ is wavelength of x-ray and β represents the full width at half maxima (FWHM), and θ represents the Bragg's diffraction angle.

Surface morphology and major elemental composition was observed by high resolution transmission electron microscopy HR-TEM, JEM 2100F, and energy dispersive spectroscopy EDS (TESCAN-VEGA3) respectively. Magnetic behavior was determined by physical property measurement system (PPMS Quantum Design, USA). Colloidal stability of NPs and hydrodynamic size was studied using Zeta-sizer Nano ZS (Malvern Instruments, 69 UK) and uniform size distribution by gel electrophoresis (GE BIORAD). Drug attachment and drug release analysis was performed with the help of UV-Vis spectroscopy (Thermo Scientific Evo 220).

4.4 Phase transfer, polymer coating and purification of MFe_2O_4 (M = Fe, Co, Ni, Zn) NPs by gel electrophoresis

The synthesis and polymer coating of NPs was carried out as previously described [33, 43]. NPs (1 ml) were mixed with 350 µl PMA (0.8M) and stirred at $60^\circ C$ for one hour. Samples were slowly dried under vacuum and finally redispersed in sodium borate buffer (SBB) pH 9. The polymer coated samples were filtered using 0.2 µm syringe filter and concentrated using centrifugal filters (Amicon Ultra-4). The concentrated samples were purified by 1% agarose gel at 100V for 90 minutes. Discrete NPs bands on the gel were cut and extracted using a 50 kDa dialysis membrane (Spectrum Laboratories, Inc.) in TBE buffer [83]. Finally, the gel extracted NPs were concentrated by using centrifuge filter and re-suspended in SBB (pH 9.0).

4.5 Preparation of drug loaded NPs

The purified polymer coated MFe_2O_4 (M = Fe, Co, Zn, Ni) NPs were further post modified with anticancer drugs; doxorubicin (DOX) and methotrexate (MTX) via EDC chemistry. NPs were incubated with optimized concentrations of EDC and drug (DOX and MTX) for two hours at room temperature. Drug attachment on NP surface was confirmed by UV-Vis spectroscopy [43]. The unbound drugs from samples were removed by 50 KDa centrifuge filters and their concentration in the waste was confirmed with the help of drug titration curves. Drug encapsulation efficiency (EE) and drug loading capacity (LC) were determined using following equations [84]:

$$Drug\ encapsulation\ efficiency\ \%$$

$$= \frac{Absorbance\ of\ drug\ used - Abosrbance\ of\ waste}{Absorbance\ of\ drug\ used} \times 100 \dots (2a)$$

$$Drug\ loading\ capacity\ \% = \frac{Entraped\ drug}{Nanoparticles\ weight} \times 100 \dots\dots\dots\dots\dots\dots\dots\dots\dots..(2b)$$

4.6 Drug release kinetics (pH dependent)

Drug release kinetics of DOX and MTX loaded MFe_2O_4 (M = Fe, Co, Zn, Ni) NPs were studied at different pH values [85]. NPs were dispersed in PBS buffer with pH values ranging from 5.5-7.4 and spectrophotometric data were measured at different time intervals (0, 1, 5, 10, 20, 40, 60 and 120 minutes). After every timepoint, samples were centrifuged at 10,000 rpm for 5 minutes and supernatants were analyzed spectrophotometrically. UV-Vis readings were analyzed with the help of DOX and MTX titration curves to estimate released drugs. Drug release % was calculated by the formula given in equation 3:

$$Drug\ release\ \% = \frac{Absorbance\ of\ supernatent}{Absorbance\ of\ drug\ loaded\ NPs} \times 100 \dots\dots\dots\dots\dots(3)$$

4.7 Cell culture

Mammalian cell lines: Human Malignant Melanoma (HT144, ATCC® HTB-63™) and Human Hepatocellular Carcinoma (HepG2, ATCC®HB-8065™) were used in this study. Cells were grown in fortified DMEM containing 10% FCS and 1% GPPS (L-glutamine 2 mM, Sodium pyruvate 1 mM, Penicillin 100 U/ml and Streptomycin 100 μg/ml) in a humidified incubator (37°C) with 10% CO_2. Cells were harvested using trypsin/EDTA (0.5 mM) for 1 minute at room temperature.

4.8 *In vitro* cytotoxicity screening of drug loaded MFe_2O_4 (M = Fe, Co, Ni, Zn) NPs

Cytotoxicity screening of colloidal drug loaded MFe_2O_4 (M = Fe, Co, Ni, Zn) NPs was performed using Sulforhodamine B (SRB) assay *in vitro* [43]. HepG2 and HT144 cells (> 90% viability, 1.5×10^5/ml) were seeded in 96-well plates (Falcon® 96-well, flat bottom, clear Microplate) and treated with 5 μg/ml of drug loaded NPs for 24 hours at 37°C followed by fixation with 50% trichloroacetic acid (TCA) for 60 minutes at 4°C. Plates were washed thrice with deionized water to remove TCA and air dried. Afterwards, SRB dye (0.05%) was added at room temperature for 30 minutes to stain cells. Excess dye was washed with 1% acetic acid 4-5 times. Plates were air dried; photographs were taken at 200X magnification with Olympus CK2 light microscope with attached camera (Optika C-B10 digital camera) and analyzed using Optika Pro View software (Version: x86, 3.7.13977.20190224). Experiment was performed twice with triplicates for all samples. Experimental controls included untreated cells (NTC), free doxorubicin (DOX), free methotrexate (MTX) and polyisobutylene-alt-maleic anhydride coated samples (NPs-PMA).

4.9 Determining IC$_{50}$ concentration of drug loaded MFe$_2$O$_4$ (M = Fe, Co, Ni, Zn) NPs

In order to determine metabolic activity and half maximal inhibitory concentration (IC$_{50}$) of drug loaded NPs, 3-(4,5-dimethylthiazol-2-yl)-2,5-diphenyl tetrazolium bromide (MTT) assay was used [83]. HepG2 and HT144 cells (> 90% viability, 1.5×10^5/ml) were exposed to varying concentrations (1, 10, 25, 50 and 100 µg/ml) of NPs for 24 hours followed by addition of MTT reagent (0.5 mg/ml) and further incubation of 4 hours. MTT reagent was solubilized overnight using 10% acidified SDS. NPs-PMA, NTC, DOX (10 µM) and MTX (10 µM) were included as controls. Non-cellular controls included media only and NPs only replicates. Absorbance at 565 nm was measured using microplate reader (FLUOstar Omega microplate reader BMG LABTECH). % cellular viabilities were calculated using following formula:

$$\% \ Viability = \frac{Absorbance \ of \ sample - Absorbance \ of \ sample \ control}{Absorbance \ of \ NTC - Absorbance \ of \ media \ only}$$
$$\times 100 \dots \dots \dots (4)$$

IC$_{50}$ values were calculated using the following formula:

$$IC50 = \frac{b - [(b - a) \ (50\% - d)]}{(c - d)} \dots \dots \dots \dots \dots . (5)$$

Where "a" and "b" are the drug concentrations producing just more than 50% and just less than 50% viable cells respectively. "c" is the percent viability produced by drug concentration "a" and "d" is the percent viability produced by drug concentration "b". Experiment was repeated twice with triplicates for each sample.

4.10 Determination of necrotic/apoptotic cells via fluorescent microscopy

In order to determine extent of apoptosis and necrosis in treated cells, acridine orange and propidium iodide fluorescent staining (AOPI) was used as previously described [43]. Pre-

seeded HepG2 and HT144 cells (> 90% viability, 1×10^5 cells/ml) were treated with drug loaded NPs (5 and 10 µg/ml) for 3 hours under appropriate culture conditions. Controls included NTC, NPs-PMA (10 µg/ml), free DOX and free MTX (5 µM each). Afterwards, cells were washed with 1X PBS and stained with AOPI (100:32 µg/ml) for 1 minute at room temperature and visualized under fluorescent microscope (200X; Nikon, MicroPhot-SA). Green fluorescence indicates viable cells, red indicate necrotic cells whereas, yellow to orange indicate early and late apoptotic cells respectively. Using Optika Pro View (Version: x86, 3.7.13977.20190224), live, necrotic and apoptotic cells were counted, and their percentages were calculated relative to NTC.

4.11 Determination of oxidative stress in treated cells

Cell-permeant 2',7'-dichlorodihydrofluorescein diacetate (H_2-DCFDA) was used to determine extent of ROS production in HepG2 and HT144 cells upon treatment with drug loaded NPs over a period of time (0-45 minutes) [86]. Briefly, cells were seeded in a 96 well plate at a density of 1.5×10^5 cells/ml under appropriate culture conditions. After 24 hours, media was removed and replaced with PBS containing 2% FCS and 25 µM H_2-DCFDA and incubated for 45 minutes. Cells were treated with NPs at IC_{50} concentrations and fluorescent intensities were recorded using microplate reader (FLUOstar Omega microplate reader BMG LABTECH) at various time points at emission and excitation wavelengths of 355/590 nm (Gain = 700). Controls included free DOX, free MTX (0.2 µM each) and NTC. Non-cellular controls included NPs only and DCF only samples. Experiment was performed in triplicates.

4.12 Cell cycle analysis

Analysis of cell cycle was performed by flow cytometry. Pre-seeded HepG2 and HT144 cells (> 90% viability, 1.5×10^5 cells/ml) were treated with IC_{50} doses of drug loaded NPs for 24

hours. Controls included NTC and free drugs (DOX and MTX = 0.2 μM each). Cells were harvested, washed with PBS and fixed in fixative solution containing 70% ethanol, 10% PBS and 20% deionized water at 4°C. For flow cytometry, fixed cells were washed with PBS and incubated with staining solution containing 50 μg/ml PI and 100 μg/ml RNase A for 30 minutes at room temperature in dark. Analysis of at least 10,000 cells was performed using flow cytometer (CytoFLEX LX flow cytometer, Beckman Coulter Life Sciences) and CytExpert software (Version 2.4) [87].

4.13 Detection of DNA strand breaks in treated cells (Alkaline comet assay)

Single cell gel electrophoresis (alkaline comet assay) was performed as described earlier [87]. HepG2 and HT144 cells (>90% viability) were exposed to drug loaded NPs at IC_{50} doses for 1 hour under standard culture conditions. Controls included NTC and free drugs (DOX and MTX = 0.2μM each). Cells were harvested, counted, embedded in 0.7% low melting agarose and spotted on comet assay slides. After solidification on ice, slides were immersed in cell lysis buffer (2.5M NaCl, 100mM Na_2-EDTA, 10mM Trizma Base pH 10, 1% sodium sarcosinate, 1% and Triton-X100) overnight at 4°C. Following day, slides were immersed in prechilled alkaline solution (0.3M NaOH, 1M Na_2-EDTA; pH 13) for 20 minutes to allow un-winding of DNA and electrophoresed for 20 minutes at 25 V and 300 mA. After air drying, staining was performed using PI (5μg/ml in PBS) and atleast 150 cells were analyzed for each sample using ImageJ software to calculate median olive tail moments relative to NTC.

4.14 Detection of DNA fragmentation in treated cells

DNA fragmentation is a hallmark of cellular apoptosis resulting in formation of small DNA fragments of 180 bp (or multiple) which can be visualized on agarose gel [88]. Ladder assay was performed using DMSO method as described previously [89]. Briefly, HepG2 and HT144

cells (> 90% viability, 1×10^5/ml) were treated with IC_{50} doses of drug loaded NPs for 24 hours at standard culture conditions. Media was removed, cells were washed with PBS and collected via trypsinization. Cellular lysis was performed by adding DMSO (100 µl) to the pellets and mixed by vortexing. Equal volume of TE buffer (pH 7.4) containing 2% SDS was added followed by vortexing. Samples were then centrifuged at 12,000 rpm for 10 minutes and resulting supernatants containing low molecular weight DNA fragments were quantified using Nanodrop 2000C. Equal amounts of DNA from all samples were electrophoresed on 2% agarose gel (containing ethidium bromide 50 µg/ml) along with Orange G dye for 2 hours at 50 V. Gel was visualized using UV transilluminator and results were recorded. Controls included NTC, DOX and MTX (30µM).

4.15 Expression assessment of Ki-67 and p53 cancer biomarkers via Immunocytochemistry (ICC)

Ki-67 and p53 protein expression was evaluated by ICC [90] (Dako EnVision[TM] FLEX detection system). HepG2 and HT144 (> 90% viability, 1.5×10^5 cells/ml) cells were cultured on sterile coverslips in 24 well plates. Cells were treated with IC_{50} doses of drug loaded NPs for 24 hours followed by fixation with TCA and washing with deionized water. Cells were immersed in antigen retrievel solution at 95°C for 45 minutes. Endogenous peroxidases were blocked by adding peroxidase blocker for 10 minutes. Ki-67 (clone MIB-1; working dilution 1:150) and p53 (clone DO-7; working dilution 1:50) mouse monoclonal antibodies were then added, and cells were incubated at 4°C overnight followed by addition of HRP conjugated secondary antibody (rabbit, polyclonal) for 30 minutes and DAB chromogen for 10 minutes to obtained desired dark brown stain with washings in between. Cells were counter stained with hematoxylin, dehydrated, mounted, and observed under light microscope (Nikon, MicroPhot-SA) at 200X magnification with attached camera (Optika C-B10 digital camera) and analyzed

45

using Optika Pro View software (Version: x86, 3.7.13977.20190224). Percentage of antibody positive cells was calculated using formula:

$$\% \, Antibody \, positive \, cells = \frac{Number \, of \, antibody \, positive \, cells}{Total \, number \, of \, cells} \, x \, 100 \, ……….(6)$$

4.16 Cytotoxicity assessment of drug loaded MFe₂O₄ (M = Fe, Co, Ni, Zn) NPs in HepG2 and HT144 3D Spheroids

Cancer cells grown in 3D cultures called spheroids, closely resemble their *in vivo* phenotype. HepG2 and HT144 spheroids were treated with drug loaded NPs (5 µg/ml) for 14 days to assess their cytotoxicity in 3D culture models. Controls included NTC and free drugs (DOX and MTX = 0.2 µM each). In brief, HepG2 and HT144 cells (> 90% viability, 5000 cells/well) were seeded in sterile, agarose coated (1.5% prepared in autoclaved deionized water; 50 µl/well) 96-well plates (Falcon® 96-well, flat bottom, clear Microplate) with 200 µl medium/well. Plates were centrifuged at 2500 rpm for 5 minutes to allow cellular accumulation in agarose meniscus. Plates were incubated at 37°C for 3 days to allow formation of closely packed 3D spheroids prior to treatment. Media was changed after every 48 hours [91]. At every timepoint, photographs were captured at 100X magnification using Olympus CK2 light microscope with attached camera (Optika C-B10 digital camera) and analyzed using Optika Pro View software (Version: x86, 3.7.13977.20190224). Average diameter of spheroids was determined using ImageJ software.

At 14th day of treatment, spheroids were collected, washed with PBS and trypsinized for 5 minutes to obtain single cell suspension. Cellular viability was then determined in triplicates using trypan blue method [92].

4.17 Assessment of Multidrug Resistance (MDR) pump activity in treated HepG2 and HT144 cells

HepG2 and HT144 exhibit intrinsic expression of ATP-binding cassette (ABC) transporters responsible for inducing multidrug resistance in response to chemotherapy [93, 94].

Here, a fluorometric MDR assay kit (ab 112142, Abcam, Cambridge, MA, USA) was used to determine MDR1 (Multidrug Resistance Protein 1) and MRP1 (Multidrug Resistance-associated Protein 1) activity in HepG2 and HT144 cells using manufacturer's protocol [95]. In brief, cells (> 90% viability, 1.5×10^5 cells/ml) were treated with drug loaded NPs at IC_{50} doses for 24 hours. Free drug controls (DOX and MTX = 0.2 µM each) and NTC were included as controls. Cyclosporin A (Cyc A = 10 µM) was included as positive control. After treatment, plates were incubated at room temperature with dye loading solution (100 µl/well) for 3 hours in dark. Fluorescent intensity relative to NTC was determined after subtracting drug only background at 485/530 nm using plate reader (FLUOstar Omega microplate reader BMG LABTECH). Higher the cellular fluorescence, higher the MDR pump inhibition. Experiment was performed in triplicates for all samples.

4.18 IC_{50} of drug loaded MFe_2O_4 (M = Fe, Co, Ni, Zn) NPs against normal cells: biocompatibility assessment *in vitro*

Cytotoxicity of drug loaded NPs was evaluated in fresh lymphocytes *in vitro*. Fresh peripheral blood (5 ml) was collected from healthy individuals in EDTA vacutainers under informed consent. Blood was diluted (1:3) with RBCs lysis buffer (155mM NH_4Cl, 0.1mM EDTA and 10mM $KHCO_3$; pH 7.2) and incubated at room temperature for 5 minutes with mixing in between, followed by centrifugation at 2000g for 5 minutes. The process was repeated 5 times to obtain clear pellet of lymphocytes [96]. Lymphocytes were resuspended in RPMI-1640

medium containing 10% FCS and 1% GPPS. Cell viability was assessed via Trypan blue method [92].

IC_{50} concentrations of drug loaded NPs were calculated by MTT assay as described earlier (section 4.9).

Funding:

References

1. Meidanchi, A.; Ansari, H. *Journal of Cluster Science* **2020**, 1-7.
2. Siegel, R. L.; Miller, K. D.; Jemal, A. *CA: a cancer journal for clinicians* **2016**, *66* (1), 7-30.
3. Kanagesan, S.; Hashim, M.; Tamilselvan, S.; Alitheen, N.; Ismail, I.; Bahmanrokh, G. *Journal of Nanomaterials* **2013**, *2013*.
4. Huang, J.; Li, H.; Chen, W.; Lv, G.-H.; Wang, X.-Q.; Zhang, G.-P.; Ostrikov, K.; Wang, P.-Y.; Yang, S.-Z. *Applied Physics Letters* **2011**, *99* (25), 253701.
5. *Seminars in cancer biology*, Elsevier: 2019.
6. Onoue, S.; Yamada, S.; Chan, H.-K. *International Journal of Nanomedicine* **2014**, *9*, 1025.
7. De Jong, W. H.; Borm, P. J. *International Journal of Nanomedicine* **2008**, *3* (2), 133.
8. Win, K. Y.; Feng, S.-S. *Biomaterials* **2005**, *26* (15), 2713-2722.

9. Wicki, A.; Witzigmann, D.; Balasubramanian, V.; Huwyler, J. *Journal of controlled release* **2015**, *200*, 138-157.

10. Issa, B.; Obaidat, I. M.; Albiss, B. A.; Haik, Y. *International journal of molecular sciences* **2013**, *14* (11), 21266-21305.

11. Chomoucka, J.; Drbohlavova, J.; Huska, D.; Adam, V.; Kizek, R.; Hubalek, J. *Pharmacological Research* **2010**, *62* (2), 144-149.

12. Giustini, A. J.; Petryk, A. A.; Cassim, S. M.; Tate, J. A.; Baker, I.; Hoopes, P. J. *Nano Life* **2010**, *1* (01n02), 17-32.

13. Rocha-Santos, T. A. *TrAC Trends in Analytical Chemistry* **2014**, *62*, 28-36.

14. Issa, B.; Obaidat, I. M. Magnetic nanoparticles as MRI contrast agents. In *Magnetic Resonance Imaging*; IntechOpen: 2019.

15. Wu, Y.; Yang, X.; Yi, X.; Liu, Y.; Chen, Y.; Liu, G.; Li, R.-W. *Journal of Nanotechnology: Nanomedicine & Nanobiotechnology* **2015**, *2* (003), 1-7.

16. Popescu, R. C.; Andronescu, E.; Vasile, B. S. *Nanomaterials* **2019**, *9* (12), 1791.

17. Srinivasan, S. Y.; Paknikar, K. M.; Bodas, D.; Gajbhiye, V. *Nanomedicine* **2018**, *13* (10), 1221-1238.

18. Sharifi, I.; Shokrollahi, H.; Amiri, S. *Journal of magnetism and magnetic materials* **2012**, *324* (6), 903-915.

19. Demortiere, A.; Panissod, P.; Pichon, B.; Pourroy, G.; Guillon, D.; Donnio, B.; Begin-Colin, S. *Nanoscale* **2011**, *3* (1), 225-232.

20. Szotek, Z.; Temmerman, W.; Ködderitzsch, D.; Svane, A.; Petit, L.; Winter, H. *Physical Review B* **2006**, *74* (17), 174431.

21. Franco Jr, A.; e Silva, F. *Applied Physics Letters* **2010**, *96* (17), 172505.

22. Gonzalez-Fernandez, M.; Torres, T.; Andrés-Vergés, M.; Costo, R.; De la Presa, P.; Serna, C.; Morales, M.; Marquina, C.; Ibarra, M.; Goya, G. *Journal of Solid State Chemistry* **2009**, *182* (10), 2779-2784.

23. Tartaj, P.; del Puerto Morales, M.; Veintemillas-Verdaguer, S.; González-Carreño, T.; Serna, C. J. *Journal of physics D: Applied physics* **2003**, *36* (13), R182.

24. Sun, S.; Zeng, H.; Robinson, D. B.; Raoux, S.; Rice, P. M.; Wang, S. X.; Li, G. *Journal of the American Chemical Society* **2004**, *126* (1), 273-279.

25. Park, S.; Lim, J.; Hwang, Y.; Kim, J.; Kim, C.; Kim, C. *physica status solidi (a)* **2007**, *204* (12), 3913-3917.

26. Peng, E.; Choo, E. S. G.; Sheng, Y.; Xue, J. M. *New Journal of Chemistry* **2013**, *37* (7), 2051-2060.

27. Mushtaq, M. W.; Kanwal, F.; Islam, A.; Ahmed, K.; Haq, Z.-u.; Jamil, T.; Imran, M.; Abbas, S. M.; Huang, Q. *Tropical Journal of Pharmaceutical Research* **2017**, *16* (7), 1663-1674.

28. Vallabani, N. V.; Singh, S.; Karakoti, A. S. *Current drug metabolism* **2019**, *20* (6), 457-472.

29. Mirza, S.; Ahmad, M. S.; Shah, M. I. A.; Ateeq, M. Magnetic nanoparticles: drug delivery and bioimaging applications. In *Metal Nanoparticles for Drug Delivery and Diagnostic Applications*; Elsevier: 2020; pp 189-213.

30. Burke, N. A.; Stöver, H. D.; Dawson, F. P. *Chemistry of materials* **2002**, *14* (11), 4752-4761.

31. Behrens, S. *Nanoscale* **2011**, *3* (3), 877-892.

32. Hong, R.; Pan, T.; Qian, J.; Li, H. *Chemical Engineering Journal* **2006**, *119* (2-3), 71-81.

33. Lin, C. A. J.; Sperling, R. A.; Li, J. K.; Yang, T. Y.; Li, P. Y.; Zanella, M.; Chang, W. H.; Parak, W. J. *Small* **2008**, *4* (3), 334-341.

34. Caballero- Díaz, E.; Pfeiffer, C.; Kastl, L.; Rivera- Gil, P.; Simonet, B.; Valcárcel, M.; Jiménez- Lamana, J.; Laborda, F.; Parak, W. J. *Particle & Particle Systems Characterization* **2013**, *30* (12), 1079-1085.

35. Soenen, S. J.; Manshian, B. B.; Abdelmonem, A. M.; Montenegro, J. M.; Tan, S.; Balcaen, L.; Vanhaecke, F.; Brisson, A. R.; Parak, W. J.; De Smedt, S. C. *Particle & Particle Systems Characterization* **2014**, *31* (7), 794-800.

36. Hochepied, J.; Pileni, M. *Journal of magnetism and magnetic materials* **2001**, *231* (1), 45-52.

37. Gambardella, P.; Rusponi, S.; Veronese, M.; Dhesi, S.; Grazioli, C.; Dallmeyer, A.; Cabria, I.; Zeller, R.; Dederichs, P.; Kern, K. *Science* **2003**, *300* (5622), 1130-1133.

38. Rondinone, A. J.; Samia, A. C.; Zhang, Z. J. *Applied Physics Letters* **2000**, *76* (24), 3624-3626.

39. Jacob, J.; Khadar, M. A. *Journal of applied physics* **2010**, *107* (11), 114310.

40. Reyes-Ortega, F.; Delgado, Á. V.; Schneider, E. K.; Checa Fernández, B.; Iglesias, G. R. *Polymers* **2018**, *10* (1), 10.

41. Kim, J.; Lawler, D. F. *Bulletin-Korean Chemical Society* **2005**, *26* (7), 1083.

42. Sabuncu, A. C.; Grubbs, J.; Qian, S.; Abdel-Fattah, T. M.; Stacey, M. W.; Beskok, A. *Colloids and Surfaces B: Biointerfaces* **2012**, *95*, 96-102.

43. Shahzad, K.; Mushtaq, S.; Rizwan, M.; Khalid, W.; Atif, M.; Din, F. U.; Ahmad, N.; Abbasi, R.; Ali, Z. *Materials Science and Engineering: C* **2020**, 111444.

44. Behzadi, S.; Serpooshan, V.; Tao, W.; Hamaly, M. A.; Alkawareek, M. Y.; Dreaden, E. C.; Brown, D.; Alkilany, A. M.; Farokhzad, O. C.; Mahmoudi, M. *Chemical Society Reviews* **2017**, *46* (14), 4218-4244.

45. Gunawan, C.; Lim, M.; Marquis, C. P.; Amal, R. *Journal of Materials Chemistry B* **2014**, *2* (15), 2060-2083.

46. Mayer, A.; Vadon, M.; Rinner, B.; Novak, A.; Wintersteiger, R.; Fröhlich, E. J. T. **2009**, *258* (2-3), 139-147.

47. Jain, S.; Bharti, S.; Bhullar, G. K.; Tripathi, S. J. M. C.; Physics. **2020**, *240*, 122162.

48. Han, U.; Seo, Y.; Hong, J. J. S. r. **2016**, *6* (1), 1-10.

49. Cha, E.-J.; Kim, J. E.; Ahn, C.-H. J. M. R. **2010**, *18* (7), 686-689.

50. Kato, Y.; Ozawa, S.; Miyamoto, C.; Maehata, Y.; Suzuki, A.; Maeda, T.; Baba, Y. *Cancer cell international* **2013**, *13* (1), 89.

51. Prabaharan, M.; Grailer, J. J.; Pilla, S.; Steeber, D. A.; Gong, S. *Biomaterials* **2009**, *30* (30), 6065-6075.

52. Patra, J. K.; Das, G.; Fraceto, L. F.; Campos, E. V. R.; del Pilar Rodriguez-Torres, M.; Acosta-Torres, L. S.; Diaz-Torres, L. A.; Grillo, R.; Swamy, M. K.; Sharma, S. *Journal of nanobiotechnology* **2018**, *16* (1), 71.

53. Kalyane, D.; Raval, N.; Maheshwari, R.; Tambe, V.; Kalia, K.; Tekade, R. K. *Materials Science and Engineering: C* **2019**, *98*, 1252-1276.

54. Kang, H.; Rho, S.; Stiles, W. R.; Hu, S.; Baek, Y.; Hwang, D. W.; Kashiwagi, S.; Kim, M. S.; Choi, H. S. *Advanced Healthcare Materials* **2020**, *9* (1), 1901223.

55. Marisca, O. T.; Kantner, K.; Pfeiffer, C.; Zhang, Q.; Pelaz, B.; Leopold, N.; Parak, W. J.; Rejman, J. *Nanomaterials* **2015**, *5* (3), 1418-1430.

56. Alhadlaq, H. A.; Akhtar, M. J.; Ahamed, M. *Cell & bioscience* **2015**, *5* (1), 55.

57. Ahamed, M.; Alhadlaq, H. A. *OncoTargets and therapy* **2014**, *7*, 269.

58. Alarifi, S.; Ali, D.; Alkahtani, S.; Alhader, M. *Biological trace element research* **2014**, *159* (1-3), 416-424.

59. Joris, F.; Valdepérez, D.; Pelaz, B.; Soenen, S. J.; Manshian, B. B.; Parak, W. J.; De Smedt, S. C.; Raemdonck, K. *Journal of nanobiotechnology* **2016**, *14* (1), 1-13.

60. Sabella, S.; Carney, R. P.; Brunetti, V.; Malvindi, M. A.; Al-Juffali, N.; Vecchio, G.; Janes, S. M.; Bakr, O. M.; Cingolani, R.; Stellacci, F. *Nanoscale* **2014**, *6* (12), 7052-7061.

61. Zhang, H.; Wang, X.; Wang, M.; Li, L.; Chang, C. H.; Ji, Z.; Xia, T.; Nel, A. E. *Small* **2015**, *11* (31), 3797-3805.

62. Yao, Y.; Zang, Y.; Qu, J.; Tang, M.; Zhang, T. *International Journal of Nanomedicine* **2019**, *14*, 8787.

63. Chiang, J. **2014**.

64. AshaRani, P.; Low Kah Mun, G.; Hande, M. P.; Valiyaveettil, S. *ACS nano* **2009**, *3* (2), 279-290.

65. Lee, T.; Lau, T.; Ng, I. *Cancer chemotherapy and pharmacology* **2002**, *49* (1), 78-86.

66. Tsurusawa, M.; Niwa, M.; Katano, N.; Fujimoto, T. *Japanese journal of cancer research* **1990**, *81* (1), 85-90.

67. Catalán, J.; Suhonen, S.; Huk, A.; Dusinska, M. Analysis of nanoparticle-induced DNA damage by the comet assay. In *Genotoxity and DNA repair*; Springer: 2014; pp 241-268.

68. Magaye, R.; Zhao, J.; Bowman, L.; Ding, M. *Experimental and therapeutic medicine* **2012**, *4* (4), 551-561.

69. Kaygisiz, Ş. Y.; Ciğerci, İ. H. *Toxicology and Industrial Health* **2017**, *33* (10), 802-809.

70. Perde-Schrepler, M.; Florea, A.; Brie, I.; Virag, P.; Fischer-Fodor, E.; Vâlcan, A.; Gurzău, E.; Lisencu, C.; Maniu, A. *Journal of Nanomaterials* **2019**, *2019*.

71. Ahamed, M.; Karns, M.; Goodson, M.; Rowe, J.; Hussain, S. M.; Schlager, J. J.; Hong, Y. *Toxicology and applied pharmacology* **2008**, *233* (3), 404-410.

72. Hong, S. C.; Lee, J. H.; Lee, J.; Kim, H. Y.; Park, J. Y.; Cho, J.; Lee, J.; Han, D.-W. *International Journal of Nanomedicine* **2011**, *6*, 3219.

73. Efeyan, A.; Serrano, M. *Cell cycle* **2007**, *6* (9), 1006-1010.

74. Pflaum, J.; Schlosser, S.; Müller, M. *Frontiers in oncology* **2014**, *4*, 285.

75. Chen, J. *Cold Spring Harbor perspectives in medicine* **2016**, *6* (3), a026104.

76. Ragab, H. M.; Samy, N.; Afify, M.; Abd El Maksoud, N.; Shaaban, H. M. *Journal of Genetic Engineering and Biotechnology* **2018**, *16* (2), 479-484.

77. Urruticoechea, A.; Smith, I. E.; Dowsett, M. *Journal of clinical oncology* **2005**, *23* (28), 7212-7220.

78. Surova, O.; Zhivotovsky, B. *Oncogene* **2013**, *32* (33), 3789-3797.

79. Daunys, S.; Janonienė, A.; Januškevičienė, I.; Paškevičiūtė, M.; Petrikaitė, V. 3D Tumor Spheroid Models for In Vitro Therapeutic Screening of Nanoparticles. In *Bio-Nanomedicine for Cancer Therapy*; Springer: 2021; pp 243-270.

80. de León Valeria, P.; Raúl, B.-R. *Cancer cell international* **2005**, *5* (1), 1-13.

81. Zöchbauer-Müller, S.; Filipits, M.; Rudas, M.; Brunner, R.; Krajnik, G.; Suchomel, R.; Schmid, K.; Pirker, R. *Anticancer research* **2001**, *21* (1A), 119-124.

82. Asati, A.; Santra, S.; Kaittanis, C.; Perez, J. M. *ACS nano* **2010**, *4* (9), 5321-5331.

83. Ali, Z.; Abbasi, R.; Khan, A.; Arshad, J.; Atif, M.; Ahmad, N.; Khalid, W. *Materials Research Express* **2018**, *5* (5), 056103.

84. Shi, Y.; Wan, A.; Shi, Y.; Zhang, Y.; Chen, Y. *BioMed research international* **2014**, *2014*.

85. Jia, H.; Kerr, L. L. *Journal of Applied Polymer Science* **2015**, *132* (7).

86. Wang, X.; Roper, M. G. *Analytical Methods* **2014**, *6* (9), 3019-3024.

87. Abbasi, R.; Efferth, T.; Kuhmann, C.; Opatz, T.; Hao, X.; Popanda, O.; Schmezer, P. *Toxicology and applied pharmacology* **2012**, *259* (3), 302-310.

88. Peitsh, M. C.; Muüller, C.; Tschopp, J. *Nucleic acids research* **1993**, *21* (18), 4206-4209.

89. Suman, S.; Pandey, A.; Chandna, S. *Cytotechnology* **2012**, *64* (1), 9-14.

90. Wan, R.; Mo, Y.; Zhang, Z.; Jiang, M.; Tang, S.; Zhang, Q. *Particle and Fibre Toxicology* **2017**, *14* (1), 38.

91. Nguyen, K.; Nuß, B.; Mühlberger, M.; Unterweger, H.; Friedrich, R. P.; Alexiou, C.; Janko, C. *Nanomaterials* **2020**, *10* (8), 1577.

92. Strober, W. *Current protocols in immunology* **1997**, *21* (1), A. 3B. 1-A. 3B. 2.

93. Roelofsen, H.; Vos, T. A.; Schippers, I. J.; Kuipers, F.; Koning, H.; Moshage, H.; Jansen, P.; Muller, M. *Gastroenterology* **1997**, *112* (2), 511-521.

94. Berger, W.; Hauptmann, E.; Elbling, L.; Vetterlein, M.; Kokoschka, E. M.; Micksche, M. *International journal of cancer* **1997**, *71* (1), 108-115.

95. Wang, X.; Li, Y.; Qian, Y.; Cao, Y.; Shriwas, P.; Zhang, H.; Chen, X. *Oncotarget* **2017**, *8* (50), 87860.

96. Dagur, P. K.; McCoy Jr, J. P. *Current protocols in cytometry* **2015**, *73* (1), 5.1. 1-5.1. 16.